THESIS

MODELING OBSERVED DEVELOPMENTAL CHANGES INFLUENCING HIPPOCAMPAL CA1 AND CA3 EPILEPTIFORM BURST CHARACTERISTICS

Submitted by

Keith A. Bush

Department of Computer Science

In partial fulfillment of the requirements

for the Degree of Masters of Science

Colorado State University

Fort Collins, Colorado

Fall 2003

COLORADO STATE UNIVERSITY

November, 2003

WE HEREBY RECOMMEND THAT THE THESIS PREPARED UNDER OUR SUPERVISION BY KEITH A. BUSH ENTITLED MODELING OBSERVED DEVELOPMENTAL CHANGES INFLUENCING HIPPOCAMPAL CA1 AND CA3 EPILEPTIFORM BURST CHARACTERISTICS BE ACCEPTED AS FULFILLING IN PART REQUIREMENTS FOR THE DEGREE OF MASTERS OF SCIENCE.

Committee on Graduate Work

Adviser

Department Head

ABSTRACT OF THESIS

MODELING OBSERVED DEVELOPMENTAL CHANGES INFLUENCING HIPPOCAMPAL CA1 AND CA3 EPILEPTIFORM BURST CHARACTERISTICS

Kainate induced epileptiform bursting recorded *in vitro* within the CA1, CA3, and Dentate Gyrus hippocampal regions of the Sprague-Dawley rat has been linked to synaptic reorganization and axonal sprouting [22, 17, 20, 21, 16, 20, 29]. Recently, Shao and Dudek [19] observed that synchronized population bursting characteristics in the CA1 and CA3 regions of the Sprague-Dawley rat change during the course of development. These changes constitute a decline in seizure susceptibility in the CA3 and CA1 regions as maturation progresses from juvenile to adult. In addition, Shao and Dudek observed that CA1 juvenile burst characteristics resemble bursting observed in the CA3 adult. Changes in population burst characteristics, driven by neural development in the CA1 and CA3 regions, strongly support the synaptic mechanism of epileptiform bursting [7] in the kainate model.

In this research, biologically-realistic computer models are used to simulate developmental changes observed by Shao and Dudek [19] in population burst characteristics between the normal juvenile and adult rat CA1 and CA3 regions under GABAergic antagonist. To recreate this developmental transformation, ranges of excitatory and inhibitory interconnections within network models comprised of 100 pyramidal cells and 9 putative interneurons are explored. Based on modeling results, CA1 development from juvenile to adult may be described by a reduction of recurrent connectivity from approximately six to two connections per pyramidal cell. Similarly, CA3 development is well-described by a recurrent connectivity reduction from approximately 30 to 20 connections per pyramidal cell.

Keith A. Bush
Department of Computer Science
Colorado State University
Fort Collins, Colorado 80523
Fall 2003

ACKNOWLEDGMENTS

This work would not be possible without the substantial input and support from my adviser Dr. Charles Anderson. Dr. F. Edward Dudek's guidance and assistance on various epileptiform topics has been invaluable. Additional thanks to Dr. Draper for accepting a position on my committee. I also thank James Knight, Li-Rong Shao, Emarit Ranu, and Todd Mytkowicz for their corrections and suggestions during preparation of this document.

TABLE OF CONTENTS

1 Introduction **1**

2 Background **3**

3 Methods **5**

3.1 CA1 and CA3 Neural Models 5

3.1.1 Channel Models 6

3.1.2 Gate Models 6

3.1.3 Shell Models 9

3.1.4 Synaptic Models 9

3.2 Putative Interneuron Model 10

3.3 Neural Model Validation Experiments 11

3.4 Network Bursting Experiments 11

3.5 Analysis of Bursting Characteristics 12

4 Validation Results **13**

4.1 CA3 Pyramidal Cells 13

4.2 CA1 Pyramidal Cells 18

4.3 Putative Interneuron 20

5 Experimental Results **25**

5.1 CA3 Population Bursting Characteristics 25

5.2 CA1 Population Burst Comparison 29

5.3 Contrasting the CA1 and CA3 regions via Modeling 32

6 Discussion **36**

7 Future Work **37**

REFERENCES **38**

A GENESIS Overview **40**

A.1 Object Reference 40

B Neuroscience Principles **42**

B.1 The Neuron 42

B.2 The Synapse 43

B.3 Neural Networks 44

C Neural Modeling Principles **45**

C.1 Membrane Potential 45

C.2 Passive Membrane Properties 47

C.2.1 Membrane Potential Temporal Rate of Change 47

C.2.2 Membrane Potential Change through Space 48

C.3 Active Membrane Properties 49

C.4 The Compartment Model 52

C.5 Synaptic Connectivity 55

C.5.1 NMDA: A voltage gated synapse 55

C.6 Solving the Discrete Compartment Model 56

C.6.1 Numerical Integration 58

C.6.2 Boundary Conditions 61

C.6.3 Solving Tridiagonal Matrices 61

C.6.4 Concentration Shells 61

C.7 Units Conversion Tables 62

LIST OF FIGURES

4.1 CA3 pyramidal cell model spontaneous bursting. 14

4.2 CA3 pyramidal cell model burst response to single depolarizing step applied to the soma. 14

4.3 CA3 pyramidal cell model response to single depolarizing step under Calcium channel blockade. 15

4.4 CA3 pyramidal cell model response to depolarizing-hyperpolarizing dual step stimulation applied at the soma. 15

4.5 CA3 pyramidal cell model firing under 0.1 nA tonic depolarization. 16

4.6 CA3 pyramidal cell model firing under 0.2 nA tonic depolarization. 17

4.7 CA3 pyramidal cell model firing under 0.4 nA tonic depolarization. 17

4.8 CA3 pyramidal cell model firing under 0.5 nA tonic depolarization. 18

4.9 CA3 pyramidal cell model response to 0.5 nA tonic depolarization applied to compartment $Apical_{16}$. 19

4.10 CA1 pyramidal cell model response to a single depolarizing step. 19

4.11 CA1 pyramidal cell model response under 0.25 nA tonic depolarization. 20

4.12 CA1 pyramidal cell model response under 0.25 nA tonic depolarization to compartment $Apical_{13}$. 21

4.13 CA1 pyramidal cell model response under 0.30 nA tonic depolarization to compartment $Apical_{16}$. 21

4.14 CA1 pyramidal cell model response under 1.25 nA tonic depolarization to compartment $Apical_{16}$. 22

4.15 Repetitive firing of PIN model at 0.01 nA tonic depolarization. 23

4.16 Repetitive firing of PIN model at 0.02 nA tonic depolarization. 23
4.17 Repetitive firing of PIN model at 0.03 nA tonic depolarization. 24
4.18 Repetitive firing of PIN model at 3.5 nA tonic depolarization. 24

5.1 Intracellular and extracellular recordings of juvenile rat CA3 region *in vitro*. 25
5.2 Intracellular and extracellular recordings of adult rat CA3 region *in vitro*. 26
5.3 Intracellular and extracellular recordings of juvenile rat CA1 region *in vitro*. 26
5.4 Extracellular recordings of adult rat CA1 region *in vitro*. 27
5.5 Example of all-or-none bursting characteristics of CA3 pyramidal cell networks. . . . 28
5.6 Example of all-or-none bursting for CA3 adult and juvenile networks. 30
5.7 Example transformation of adult to juvenile CA1 burst characteristics. 31
5.8 Graded population bursting of CA1 networks at low connectivity. 33
5.9 Graded population bursting of CA1 networks at moderate connectivity. 34
5.10 Comparison of CA1 and CA3 network burst characteristics at equivalent connectivity levels. 35

B.1 Generalized depiction of a neuron. 43

C.1 Membrane potential temporal response to current perturbation. 48
C.2 Membrane potential decay with respect to spatial location. 49
C.3 Computer model of Hodgkin-Huxley voltage-clamp experiment in which Na channels are blocked. 50
C.4 Computer model of Hodgkin-Huxley derived voltage-clamp trace of squid axon when K channels are blocked. 50
C.5 Voltage dependent behavior of gate activation and inactivation variable rates of change and steady state permissiveness. 53
C.6 Schematic of a generalized compartment model. 53
C.7 Graphical representation of a complex neural membrane equivalent circuit. 54
C.8 Synaptic channel conductance behavior as g_{max} and τ are varied. 56

LIST OF TABLES

3.1 CA3 voltage-gated ion channel conductance densities in SI units. 6
3.2 CA1 voltage-gated ion channel conductance densities in SI units. 7
3.3 Putative Interneuron voltage-gated ion channel conductance densities in SI units. . . 10

Chapter 1

Introduction

Epilepsy, by definition, is the propensity to have seizures. The neuronal firing patterns leading to epileptic symptoms, seizures, are called epileptiform bursting. Epileptiform bursts take the form of large-scale, network-synchronized signals. Epileptogenesis is a broad term used to describe structural and physiological abnormalities in the nervous system resulting in chronic epilepsy [7, 6].

It is widely accepted that epileptiform discharges in the brain are rooted in increased excitatory neural connections coupled with or in lieu of increased neural network inhibition. Research attempting to identify the underlying aetiology has made substantial progress. Rather than narrow potential fundamentals, however, this research has generated numerous plausible models of both epileptiform generation and mechanisms of epilepsy. Epileptogenesis taxonomy roughly divides models into two categories, synaptic and non-synaptic. Synaptic models are further divided into excitatory and inhibitory models. Non-synaptic models divide into those relying on gap junction effects, field effects, and changes in the ionic properties of the extracellular space. Additionally, three competing models of epileptiform generation have been proposed: recurrent connectivity signaling, intrinsic signaling and spread, and emergent signaling from distributed networks [7].

The synaptic mechanism of epilepsy proposes that epileptogenesis is caused by abnormal structural changes in the synaptic connections of neural structures not typically exhibiting epileptiform bursting. Newly formed connections have the ability to unbalance and override the inhibitory-induced equilibrium of the network structure. It has been proposed that this imbalance is an important element of mossy fiber sprouting induced epileptiform bursting. Motivation for this model is substantial. Abnormal synaptic connectivity may be attributed to regrowth in the wake of neural tissue death as a result of traumatic injury, surgical procedure, and repeated exposure to convulsant agents [7]. Neuronal death in the hippocampus, induced by trauma injuries, has been linked to epileptogenesis [7]. Further, surgical procedures have been shown to both induce and ameliorate epileptiform bursting in neural tissue [7]. It is thought that surgical trauma of neural tissue may respectively induce new connectivity or sever previously hyper-excitable network structures.

The kainate-model, the artificial inducement of status epilepticus and epileptogenesis in a Sprague-Dawley rat via subcutaneous injection of kainic acid, is a highly successful animal model used in the study of the synaptic mechanism of epilepsy [17]. Kainic acid injection elicits a three-part response in the rat subject: 1) short-term status epilepticus, 2) variable length latent period, and 3) onset of epileptogenensis. *In vitro* slice experiments performed on hippocampal tissue removed from kainate treated rats has facilitated study of the role neural structure and behavior in epileptogenesis. Kainate-model epileptiform bursts recorded *in vitro* within the CA1, CA3, and dentate gyrus hippocampal regions of the Sprague-Dawley rat have been linked to synaptic reorganization and axonal sprouting [22, 17, 20, 21, 16, 20, 29].

Recently, Shao and Dudek [19] observed that population burst characteristics in the CA1 and CA3 regions change during development in ways that oppose the onset of epileptogenesis. Changes in bursting during development may be characterized by a decline in seizure susceptibility in the CA3 and CA1 regions as maturation progresses from juvenile to adult. In addition, Shao and Dudek observed that CA1 juvenile burst characteristics resemble bursting observed in the CA3 adult [19].

This evidence suggests that synaptic reorganization may occur during rat hippocampal development and is a fundamental component of epileptiform bursting differences observed between the juvenile and adult hippocampi [19]. Developmental synaptic reorganization may also serve as a corollary between changes in normal rat population burst changes and those induced by the kainate-model.

The research presented in this paper models, via computer simulation, developmental changes observed by Shao and Dudek [19] in population burst characteristics from the normal juvenile to the adult rat CA1 and CA3 regions under GABAergic antagonist. Suppression of GABAergic inhibition (i.e. fast $GABA_A$ blockade via bicuculline) is generally necessary to unmask excitatory glutamatergic pathways during hippocampal slice experimentation [17]. To recreate this developmental transformation, ranges of excitatory and inhibitory interconnections within network models comprised of 100 pyramidal cells and 9 putative interneurons are explored. Membrane potential recordings and network-firing activity plots best matching *in vitro* recordings [19] are presented along with corresponding connectivity densities.

The construction of a recurrent connectivity model of normal Sprague-Dawley Rat CA1 development is novel. This model lends substantial support to the proposed role of synaptic reorganization in population bursting of normal CA1 and CA3 regions. A synaptic model of rat hippocampal development and related burst characteristics supports an explanation of epileptiform bursting induced by the kainate model via a similar mechanism. This work establishes a base for further research in the role of synaptic reorganization in dentate gyrus epileptiform bursting.

The remainder of this paper is organized as follows. Chapter 2 presents related work and background material. Experimental methodology is defined in Chapter 3. Results of validation experiments are presented in Chapter 4. CA1 and CA3 burst results are presented in Chapter 5. Discussion of the results and future work can be found in Chapters 6 and 7, respectively. A brief overview of the GENESIS [4] language is provided in Appendix A. Introduction to fundamental neuroscience topics and computational neuroscience principles are provided in Appendices B and C, respectively.

Chapter 2

Background

Evidence from electrophysiological recordings of kainate-treated rats [22, 17, 20, 21], pilocarpine-induced status epilepticus rats, and human, surgical, temporal-lobe epilepsy patients suggest that CA1 and CA3 pyramidal cells, as well as dentate granule cells, undergo axonal sprouting and synaptic reorganization in response to neuronal death [16, 20]. Electrophysiological evidence for synaptic reorganization is substantial. Increased synchronous population-burst characteristics are observed when γ-aminobutyric acid-A ($GABA_A$) mediated inhibition is blocked via bicuculline [16, 20]. Under bicuculline $GABA_A$ disinhibition, the nature of synchronous population bursting within the kainate model for CA1, CA3, and dentate granule cells is characterized by a greater number and duration of bursts as well as an all-or-none bursting in response to afferent stimulation [16, 17, 20, 21]. All-or-none bursting phenomena observed in kainate-treated CA1 and CA3 regions are robust against superthreshold stimulation in contrast with graded bursting at integer multiples of threshold stimulation in control [20].

Rats treated with kainic-acid display hippocampal neuronal death, particularly in the CA1, CA3, and dentate regions [1, 3, 5]. Nissl staining has shown significant, temporally progressive death of CA1 pyramidal cells and putative inhibitory interneurons in response to kainate treatment. This cell death has been correlated with increased synchronous population bursting [21]. Digital reconstruction of CA1 pyramidal cells at intervals after kainate treatment have shown significant increases in axon length and branching. Timm stain intensity in the inner molecular layer, evidence of axonal sprouting, has been correlated with increased excitatory post-synaptic potential (EPSP) amplitude and frequency in kainate-treated dentate granule cells [29]. Granule cell axons of kainate-treated rats have been shown to be longer compared to control [5].

The evidence presented above supports a hypothetical model of epileptogenesis in which chronic, spontaneous electrographic epileptiform bursting is induced by the kainate-treated rat model. It is proposed that kainic acid injection immediately induces status epilepticus through suppression of inhibitory interneurons (either via neural death or another mechanism). Long-term recovery of inhibition introduces a latent period, a period characterized by low probability of spontaneous epileptiform bursting. During the latent period, slow-acting anatomical changes in the CA1, CA3 and dentate gyrus, thought to include axonal sprouting and excitatory synaptic reorganization, occur. While not directly observed, the synchronized population bursting exhibited by kainate-treated rat CA1, CA3, and dentate granule cells contain characteristics of increased recurrent excitatory connectivity that are supported via detailed CA3 and dentate granule cell model simulations [28, 18, 14] as well as CA3 statistical models [24, 23, 2].

Recent data reported by Shao and Dudek [19] suggest that, during development, synaptic reorganization occurs in the male, Sprague-Dawley rat CA1 region. Electrographic recordings of CA1 pyramidal cells under GABAergic antagonist suggest that the normal juvenile rat CA1 region displays synchronized population bursts with characteristics similar to the normal adult rat CA3. This behavior is characterized by all-or-none bursting in response to increasing levels of afferent stimulation with decreasing latency. Synchronized population bursts in the normal rat CA1 diminish as rat development reaches maturation and the all-or-none bursting property is replaced by a graded burst

response. A parallel trend is observed in the CA3 region. The probability of observing all-or-none bursting in the CA3 decreases as development progresses. In addition, the intensity and duration of bursts is significantly more pronounced in the juvenile CA3 as compared to the adult CA3. This evidence strongly suggests that recurrent excitatory connectivity in the CA1 and CA3 regions plays a fundamental role in population burst characteristics.

Chapter 3

Methods

Traub's [28] CA1 and CA3 pyramidal cell models are used as the basis for neurons modeled in this research. The GENESIS environment will serve as the primary simulation platform. Adaptations of Traub's models for use in GENESIS are based on the models of Beeman [4]. Traub's original parameters and kinetic forms were followed as closely as possible. All units and derivations have been transformed to conform to SI units. All derivations and kinetic equations have been re-reported here to avoid confusion due to the numerical disruption that units conversion has on kinetic equations, as well as the differences in the canonical GENESIS format for model derivations with respect to original Traub derivations. Model specifications, as they are incorporated into the GENESIS environment, are presented below. Deviations from the Traub parameters and derived equations are noted when necessary in order to facilitate complete validation of this work.

In this section, each of the three neural models, CA1, CA3, and PIN will be described in detail. Mathematical descriptions of the compartment models making up these neurons, including synaptic connection models, channel models, and ionic concentration shell models will also be detailed as will all underlying membrane parameter and channel density assumptions.

3.1 CA1 and CA3 Neural Models

CA1 and CA3 models are comprised of 19 compartments. Compartments 1–8 are basilar dendritic compartments, compartment 9 is the soma, and compartments 10–19 are the apical dendritic compartments. All compartments are modeled as cylinders having the following specific membrane properties: $C_M = 0.003\ F/m^2$, $R_A = 1.0\ Ohm \cdot m$, and $R_M = 0.1\ Ohm \cdot m^2$. Apical compartments have length $120 \times 10^{-6}\ m$ and diameter $5.78 \times 10^{-6}\ m$. Length and diameter of the soma are $125 \times 10^{-6}\ m$ and $8.46 \times 10^{-6}\ m$, respectively. Basilar dendrite length and diameter parameters are $110 \times 10^{-6}\ m$ and $4.84 \times 10^{-6}\ m$, respectively. Compartment anatomical and membrane parameters are identical for both CA1 and CA3 models.

The derivative of the discretized membrane potential with respect to time, $\frac{dV_i}{dt}$, was computed as a Taylor series approximation to the cable model with sealed-end boundary conditions:

$$C_{m_i}\frac{dV_i}{dt} = \frac{V_{i-1} - V_i}{R_{a_{i-1}}} + \frac{V_{i+1} - V_i}{R_{a_i}} + \frac{V_i}{R_{m_i}} + I_{ionic_i} + I_{inject_i} \tag{3.1}$$

where V_i is the membrane potential of compartment i, I_{ionic_i} is the current contribution of active-gated channels and synaptic channels within compartment i, and I_{inject_i} represents external current injected to compartment i. In accordance with canonical GENESIS format, membrane potential diffusion between compartments is approximated using axial resistance, R_a, rather than conductance as used by Traub [28]. Also, the ionic leak conductance reported by Traub [28] as $0.1\ mS/cm^2$ has been reformed as ionic leak resistance in terms of the membrane resistance, R_M, as is the standard form for the GENESIS environment. To eliminate spontaneous action potentials, membrane resistance was reduced to $0.5\ Ohm \cdot m^2$ and $0.7\ Ohm \cdot m^2$ for the CA3 and CA1 models, respectively. Rest potential, E_{rest}, for both CA1 and CA3 models was $-0.060\ Volts$.

Specific Channel Conductance Densities S/m^2							
Comp	Name	g_{Na}	g_{Ca}	$g_{K(DR)}$	g_{KAHP}	g_{KC}	g_{KA}
1	$Basal_1$	0.0	0.0	0.0	0.0	0.0	0.0
2	$Basal_2$	0.0	50.0	0.0	8.0	0.0	0.0
3	$Basal_3$	0.0	50.0	0.0	8.0	0.0	0.0
4	$Basal_4$	0.0	120.0	0.0	8.0	0.0	0.0
5	$Basal_5$	0.0	120.0	0.0	8.0	0.0	0.0
6	$Basal_6$	200.0	120.0	200.0	8.0	0.0	0.0
7	$Basal_7$	0.0	50.0	0.0	8.0	0.0	0.0
8	$Basal_8$	150.0	80.0	50.0	8.0	0.0	0.0
9	$Soma$	300.0	40.0	150.0	8.0	5.0	50.0
10	$Apical_{10}$	150.0	80.0	50.0	8.0	0.0	0.0
11	$Apical_{11}$	0.0	50.0	0.0	8.0	0.0	0.0
12	$Apical_{12}$	20.0	170.0	200.0	8.0	0.0	0.0
13	$Apical_{13}$	0.0	170.0	0.0	8.0	0.0	0.0
14	$Apical_{14}$	0.0	170.0	0.0	8.0	0.0	0.0
15	$Apical_{15}$	0.0	100.0	0.0	8.0	0.0	0.0
16	$Apical_{16}$	0.0	100.0	0.0	8.0	0.0	0.0
17	$Apical_{17}$	0.0	50.0	0.0	8.0	0.0	0.0
18	$Apical_{18}$	0.0	50.0	0.0	8.0	0.0	0.0
19	$Apical_{19}$	0.0	0.0	0.0	0.0	0.0	0.0

Table 3.1: CA3 voltage-gated ion channel conductance densities in SI units.

3.1.1 Channel Models

The membrane current flow, I_{ionic_i}, in compartment i due to actively-gated and synaptic-gated channels is modeled by:

$$\begin{aligned} I_{ionic_i} &= \bar{g}_{Na_i} m_i^2 h_i (E_{Na} - V_i) + \bar{g}_{Ca_i} s_i^2 r_i (E_{Ca} - V_i) + \\ &\quad \bar{g}_{KDR_i} n_i (E_K - V_i) + \bar{g}_{KA_i} a_i b_i (E_K - V_i) + \bar{g}_{KAHP_i} q_i (E_K - V_i) + \\ &\quad \bar{g}_{KC} c_i z_i (E_K - V_i) + I_{synaptic_i} \end{aligned} \tag{3.2}$$

Six channel models determine the actively-gated ionic influences of the compartment: Na, Ca, KDR, $KAHP$, KA, and KC. E_{Na}, E_{Ca}, and E_K represent the reversal potentials of Na^+, Ca^{2+}, and K^+ ionic species, which are fixed at values 0.055, 0.080, and $-0.075\,Volts$, respectively. $I_{synaptic_i}$ represents the sum of current contributions of synaptic-gated ion channels for compartment i as given in Equation 3.3. Definitions of I_{AMPA_i} and I_{NMDA_i} are provided in Equations 3.27 and 3.29, respectively. Definitions of $I_{GABA_{A_i}}$ and $I_{GABA_{B_i}}$ are provided in Equations 3.32 and 3.34, respectively.

$$I_{synaptic_i} = I_{AMPA_i} + I_{NMDA_i} + I_{GABA_{A_i}} + I_{GABA_{B_i}} \tag{3.3}$$

It should be noted that $\bar{g}_{chan}$ quantities represent absolute conductances (S). Conversion from specific to absolute conductance was achieved using equation Equation 3.4, where d_i and l_i represent the diameter and length of compartment i, respectively. Specific conductances for all channels over all compartments are given by Tables 3.1 and 3.2 for the CA3 and CA1 models, respectively.

$$\bar{g}_{chan_i} = g_{chan_i} \pi d_i l_i \tag{3.4}$$

3.1.2 Gate Models

Channel gating kinetics, as depicted in Equation 3.5 are linear. As is standard form, forward, α, and backward, β, gate variables are functions of ψ, where ψ represents either V_i or $\chi_{Ca,i}$ depending

Specific Channel Conductance Densities S/m^2							
Comp	Name	g_{Na}	g_{Ca}	$g_{K(DR)}$	g_{KAHP}	g_{KC}	g_{KA}
1	$Basal_1$	0.0	0.0	0.0	0.0	0.0	0.0
2	$Basal_2$	0.0	50.0	0.0	8.0	50.0	0.0
3	$Basal_3$	0.0	50.0	0.0	8.0	50.0	0.0
4	$Basal_4$	0.0	70.0	0.0	8.0	50.0	0.0
5	$Basal_5$	0.0	70.0	0.0	8.0	50.0	0.0
6	$Basal_6$	200.0	120.0	200.0	8.0	100.0	0.0
7	$Basal_7$	0.0	50.0	50.0	8.0	50.0	0.0
8	$Basal_8$	150.0	80.0	100.0	8.0	200.0	0.0
9	$Soma$	300.0	40.0	250.0	8.0	100.0	50.0
10	$Apical_{10}$	150.0	80.0	100.0	8.0	200.0	0.0
11	$Apical_{11}$	0.0	50.0	50.0	8.0	50.0	0.0
12	$Apical_{12}$	20.0	170.0	200.0	8.0	150.0	0.0
13	$Apical_{13}$	0.0	70.0	0.0	8.0	50.0	0.0
14	$Apical_{14}$	0.0	70.0	0.0	8.0	50.0	0.0
15	$Apical_{15}$	0.0	70.0	0.0	8.0	50.0	0.0
16	$Apical_{16}$	0.0	50.0	0.0	8.0	50.0	0.0
17	$Apical_{17}$	0.0	50.0	0.0	8.0	50.0	0.0
18	$Apical_{18}$	0.0	50.0	0.0	8.0	50.0	0.0
19	$Apical_{19}$	0.0	0.0	0.0	0.0	0.0	0.0

Table 3.2: CA1 voltage-gated ion channel conductance densities in SI units.

on the nature of the channel gated—$\chi_{Ca,i}$ denotes concentration of Ca^{2+} ions within compartment i. Equations 3.6-3.25 present α and β gate variable equations for both activation and inactivation gates of the channels specified in Equation 2. The equations are given in GENESIS standard form using SI units but are based on equations originally presented by Traub [28].

$$\frac{dp_i}{dt} = \alpha_{p_i}(\psi)(1 - p_i) - \beta p_i(\psi_i)p_i \tag{3.5}$$

$$m_{\alpha,i} = \frac{320 \times 10^3 (0.0131 + E_{rest}) - 320 \times 10^3 V_i}{-1 + \exp\left(\frac{V_i - (0.0131 + E_{rest})}{-0.004}\right)} \tag{3.6}$$

$$m_{\beta,i} = \frac{-280 \times 10^3 (0.0401 + E_{rest}) + 280 \times 10^3 V_i}{-1 + \exp\left(\frac{V_i - (0.0401 + E_{rest})}{5.0 \times 10^{-3}}\right)} \tag{3.7}$$

$$h_{\alpha,i} = \frac{128.0}{\exp\left(\frac{V_i - (0.017 + E_{rest})}{0.018}\right)} \tag{3.8}$$

$$h_{\beta,i} = \frac{4.0 \times 10^3}{1 + \exp\left(\frac{V_i - (0.040 + E_{rest})}{-5.0 \times 10^{-3}}\right)} \tag{3.9}$$

$$s_{\alpha,i} = \frac{1.6 \times 10^3}{1.0 + \exp\left(\frac{V_i - (0.065 + E_{rest})}{-0.01389}\right)} \tag{3.10}$$

$$s_{\beta,i} = \frac{-20 \times 10^3 (0.0511 + E_{rest}) + 20 \times 10^3 V_i}{-1 + \exp\left(\frac{V_i - (0.0511 + E_{rest})}{5.0 \times 10^{-3}}\right)} \tag{3.11}$$

$$r_{\alpha,i} = \begin{cases} 5.0, & \text{if } V_i \leq E_{rest} \\ 5.0\left(\exp\left(-50(V_i - E_{rest})\right)\right), & \text{if } V_i > E_{rest} \end{cases} \tag{3.12}$$

$$r_{\beta,i} = 5.0 \tag{3.13}$$

$$n_{\alpha,i} = \frac{16 \times 10^3 (0.0351 + E_{rest}) - 16 \times 10^3 V_i}{-1 + \exp\left(\frac{V_i - (0.0351 + E_{rest})}{-0.005}\right)} \tag{3.14}$$

$$n_{\beta,i} = \frac{250}{\exp\left(\frac{V_i - (0.02 + E_{rest})}{0.04}\right)} \tag{3.15}$$

$$a_{\alpha,i} = \frac{20 \times 10^3 (0.0131 + E_{rest}) - 20 \times 10^3 V_i}{-1 + \exp\left(\frac{V_i - (0.0131 + E_{rest})}{-0.01}\right)} \tag{3.16}$$

$$a_{\beta,i} = \frac{-17.5 \times 10^3 (0.0401 + E_{rest}) + 17.5 \times 10^3 V_i}{-1 + \exp\left(\frac{V_i - (0.0401 + E_{rest})}{0.01}\right)} \tag{3.17}$$

$$b_{\alpha,i} = \frac{1.6}{\exp\left(\frac{V_i + (0.013 + E_{rest})}{0.018}\right)} \tag{3.18}$$

$$b_{\beta,i} = \frac{50.0}{1 + \exp\left(\frac{V_i - (0.0101 + E_{rest})}{-0.005}\right)} \tag{3.19}$$

$$q_{\alpha,i} = \begin{cases} 0.02\chi_{Ca,i}, & \text{if } \chi_{Ca,i} < 500.0 \\ 10.0, & \text{if } \chi_{Ca,i} \geq 500.0 \end{cases} \tag{3.20}$$

$$q_{\beta,i} = q_{\alpha,i} + 1.0 \tag{3.21}$$

$$c_{\alpha,i} = \begin{cases} \frac{\exp(53.872(V_i - E_{rest}) - 0.66835)}{0.018975}, & \text{if } V_i \leq E_{rest} + 0.050 \\ 2000\exp\left(\frac{E_{rest} + 0.0065 - V_i}{0.027}\right), & \text{if } V_i > E_{rest} + 0.050 \end{cases} \tag{3.22}$$

$$c_{\beta,i} = \begin{cases} c_{\alpha,i} + 2000\exp\left(\frac{E_{rest} + 0.0065 - V_i}{0.027}\right), & \text{if } V_i \leq E_{rest} + 0.050 \\ c_{\alpha,i}, & \text{if } V_i > E_{rest} + 0.050 \end{cases} \tag{3.23}$$

$$z_{\alpha,i} = \begin{cases} \chi_{Ca,i}/250, & \text{if } \chi_{Ca,i} < 250.0 \\ 1.0, & \text{if } \chi_{Ca,i} \geq 250.0 \end{cases} \tag{3.24}$$

$$z_{\beta,i} = 1.0 \tag{3.25}$$

3.1.3 Shell Models

In both CA1 and CA3 neural models, compartments 2–18 contain shell models that approximate Ca^{2+} concentration within proximity to the compartment membrane surface such that these concentrations affect concentration-gated ion channels. Shells are omitted from compartments 1 and 19 as Ca^{2+}-dependent channel conductances are absent [28]. Due to largely unknown intracellular Ca^{2+} kinetics (i.e., axial and radial diffusion rates), shell concentrations should be viewed as model abstractions to approximate gross $[Ca^{2+}]$ response to potential changes effected in the compartments. Equation 3.26 depicts the Ca^{2+} shell concentration kinetic approximation.

$$\frac{d\chi_{Ca,i}}{dt} = \phi_{Ca,i} I_{Ca,i} + \frac{\chi_{Ca,i}}{\tau_{Ca,i}} \tag{3.26}$$

The value of calcium decay, $\tau_{Ca,i}$, was fixed to be 0.01333 sec [4]. The scaling factors used to convert Ca^{2+} current into intracellular concentrations are as follows [4]: $\phi_{Ca,i} = 7.769 \times 10^{12}$ $i = 2, ..., 7$; $\phi_{Ca,i} = 34.53 \times 10^{12}$, $i = 8$; $\phi_{Ca,i} = 17.402 \times 10^{12}$, $i = 9$; $\phi_{Ca,i} = 26.404 \times 10^{12}$, $i = 10$; and $\phi_{Ca,i} = 5.941 \times 10^{12}$, $i = 11, ..., 18$. It should be noted that the units of these conversions are arbitrary in that the radial width implied for the shells is undetermined.

3.1.4 Synaptic Models

As given by Traub [28], fast and slow acting, excitatory synaptic ionic influences are present. The QUIS synaptic alpha model proposed by Traub has been replaced by a dual-exponential AMPA model. Equation 3.28 depicts the temporal kinetics of the AMPA model. Rise and decay time constants were fit to conform to the 2 ms constraints given by Traub [28]. Reversal potential of the AMPA synapse, E_{AMPA}, is set to 0.0 $Volts$. Values τ_{AMPA_1} and τ_{AMPA_2} are 2×10^{-3} sec [14].

$$I_{AMPA_i} = \bar{g}_{AMPA_i}(E_{AMPA} - V_i), \; i = 3, 15 \tag{3.27}$$

$$\bar{g}_{AMPA_i} = \frac{g_{AMPA}}{\tau_{AMPA_1} - \tau_{AMPA_2}} \left(e^{-t/\tau_{AMPA_1}} - e^{-t/\tau_{AMPA_2}} \right) \tag{3.28}$$

The slow excitatory NMDA model proposed by Traub [28], in GENESIS form, is described by Equations 3.29-3.31. This synapse is voltage dependent and limited by Mg^{2+}. The model's temporal form has been fit to a rise and decay time of 100 ms [28]. NMDA reversal potential, E_{NMDA}, is 0.0 $Volts$. Values τ_{NMDA_1} and τ_{NMDA_2} are 100×10^{-3} and 80×10^{-3} sec, respectively [14].

$$I_{NMDA_i} = \bar{g}_{NMDA_i}(E_{NMDA} - V_i), \text{ for } i = 15 \tag{3.29}$$

$$\bar{g}_{NMDA} = \frac{g_{NMDA}}{\tau_{NMDA_1} - \tau_{NMDA_2}} \left(e^{-t/\tau_{NMDA_1}} - e^{-t/\tau_{NMDA_2}} \right) \cdot r_{Mg} \tag{3.30}$$

$$r_{Mg} = \frac{1}{1 + \eta \cdot [Mg^{2+}] \cdot e^{-V_i \gamma}} \tag{3.31}$$

The values of $\bar{g}_{AMPA}$ and $\bar{g}_{NMDA}$ are scaling factors for the maximal synaptic conductance ($Siemens$). Time, t (sec), denotes simulation time passed since activation of the synaptic receptor. In accordance with Traub [28], an excitatory postsynaptic potential (EPSP) for a single action potential is defined as activation of the fast AMPA synaptic receptors located in compartments 3 and 15 as well as the slow NMDA receptor located in compartment 15. Action potentials originate within the soma compartment exclusively. The threshold for action potential is 0.0 $Volts$. Axonal propagation velocity is defined as 1.0 m/sec [13].

Putative interneurons provide inhibition to pyramidal cells through both fast, $GABA_A$, and slow, $GABA_B$, inhibitory synaptic connections. Kinetics for the $GABA_A$ model are defined by Equations 3.32 and 3.33. E_{GABA_A} was -0.068 $Volts$. Values $\tau_{GABA_{A_1}}$ and $\tau_{GABA_{A_2}}$ are 2×10^{-3} and 1×10^{-3} sec, respectively. $GABA_B$ kinetics are defined by Equations 3.34 and 3.35. E_{GABA_B} is -0.088 $Volts$. Values $\tau_{GABA_{B_1}}$ and $\tau_{GABA_{B_2}}$ are 100×10^{-3} and 67×10^{-3} sec, respectively [14].

PIN specific conductance densities (S/m^2) and dimensions (m)								
Comp	Name	g_{Na}	g_{Ca}	$g_{K(DR)}$	g_{KC}	g_{KA}	length	diam
1	$Soma$	1000.0	10.0	1350.0	200.0	5.0	20.0	15.0
2	$SD6$	250.0	10.0	250.0	80.0	5.0	50.0	1.88
3	$SD7B$	500.0	10.0	500.0	40.0	0.0	50.0	1.88
4	$SD7A$	500.0	10.0	500.0	40.0	0.0	50.0	1.20
5	$SD8B$	250.0	10.0	250.0	40.0	0.0	50.0	1.88
6	$SD8A$	250.0	10.0	250.0	40.0	0.0	50.0	1.20

Table 3.3: Putative Interneuron voltage-gated ion channel conductance densities in SI units.

Time, t, is defined as above.

$$I_{GABA_{A_i}} = \bar{g}_{GABA_{A_i}} \left(E_{GABA_A} - V_i\right), \text{ for } i = 8, 10 \tag{3.32}$$

$$\bar{g}_{GABA_{A_i}} = \frac{g_{GABA_{A_i}}}{\tau_{GABA_{A_1}} - \tau_{GABA_{A_2}}} \left(e^{-t/\tau_{GABA_{A_1}}} - e^{-t/\tau_{GABA_{A_2}}}\right) \tag{3.33}$$

$$I_{GABA_{B_i}} = \bar{g}_{GABA_{B_i}} (E_{GABA_B} - V_i), \; i = 10 \tag{3.34}$$

$$\bar{g}_{GABA_{B_i}} = \frac{g_{GABA_{B_i}}}{\tau_{GABA_{B_1}} - \tau_{GABA_{B_2}}} \left(e^{-t/\tau_{GABA_{B_1}}} - e^{-t/\tau_{GABA_{B_2}}}\right) \tag{3.35}$$

Values of $\bar{g}_{GABA}$ and t are defined earlier. An inhibitory postsynaptic potential (IPSP) coinciding with a single action potential is defined as activation of $GABA_A$ synaptic receptors located in compartments $Basal_8$ and $Apical_{10}$ as well as a $GABA_B$ synaptic receptor in compartment $Apical_{10}$. The close proximity of inhibitory receptors to the soma is intended to maximize inhibitory effect on burst generation in the soma. Inhibitory receptor placement also symmetrically opposes, in terms of fast and slow activation time, the excitatory synaptic inputs of the dendritic tree [26].

3.2 Putative Interneuron Model

To facilitate inhibitory synaptic signaling, a putative interneuron (PIN) model was developed. The six compartment PIN model is intended to mimic the function of a 45 compartment interneuron model proposed by Traub, et al. [27]. The PIN model contained six compartments defining a single dendritic branch and soma of the original model, such that original electronic lengths were maintained [27]. For all compartments, $R_M = 5.0\ \Omega m^2$, $R_A = 2.0\ \Omega m$ and $C_M = 0.0075\ F/m^2$. Rest potential, E_{rest}, for all compartments is $-0.060\ Volts$. These values closely follow original model parameters [27]. All compartments are modeled as cylinders. Compartment dimensions are defined by values in Table 3.3.

Like the CA1 and CA3 models, membrane current of PIN compartments were calculated by Equation 3.1. However, $KAHP$ channels are not incorporated into the PIN model. Specific channel conductance densities are presented in Table 3.3. Calcium concentration shell models follow those of CA1 and CA3, given by Equation 3.26. For all compartments, $\phi_{Ca,i}$ is 5.941×10^{12} and $\tau_{Ca,i}$ is 0.333 [27].

The kinetics of all channels were identical to those used in the CA1 and CA3 neural models as defined by Equations 3.6-3.25. An EPSP in the PIN model was defined as the simultaneous activation of both $AMPA$ and $NMDA$ glutamatergic receptors located at compartment named $SD8A$[1]. Recurrent inhibition of interneurons is not included in the model due to the lack of sufficient biological data. $AMPA$ and $NMDA$ currents in the PIN model are defined analogous to pyramidal cells by Equations 3.27 and 3.29, respectively.

[1] PIN neuron nomenclature is defined to coincide with the original convention defined by Traub, et al. [27]

3.3 Neural Model Validation Experiments

Validation experiments were performed on both the Traub CA1 and CA3 models as well as the PIN model. Validation experiments are necessary to ensure that implementations of the neural models in GENESIS do not contain coding or unit conversion errors. Second, these validation experiments are used to ensure that modifications to the original model specifications did not significantly change gross firing behaviors originally observed by Traub [28]. The preservation of firing characteristics will be detailed in Section 4.

The CA1 model was simulated under the following five stimulus conditions: 3.0 nA, 5 ms depolarizing step applied to the *Soma* compartment, 0.25 nA tonic depolarization applied to compartment $Apical_{13}$, 0.25 nA tonic depolarization applied to the *Soma* compartment, 0.30 tonic depolarization applied to compartment $Apical_{16}$, and 1.25 nA tonic depolarization applied to compartment $Apical_{16}$. All depolarizing stimuli were applied 25 ms after the start of the simulation. Data for step depolarization simulations was collected at 0.05 ms time intervals for 300 ms. Data for tonic depolarization were collected at 0.05 ms time intervals for 3.0 s. Membrane potential was simultaneously recorded from the *Soma*, $Apical_{13}$, and $Apical_{16}$ compartments, respectively.

Nine experimental configurations were used for CA3 model validation: 3.0 nA, 5 ms depolarizing step applied to the *Soma*, successive 3.0 nA depolarizing and 3.0 nA hyperpolarizing 5 ms steps applied to the *Soma* compartment, tonic depolarizations applied to the *Soma* compartment over the range of [0.1,0.5] nA at intervals of 0.1 nA, 1.5 nA tonic depolarization applied to compartment $Apical_{16}$, and 3.0 nA, 5 ms depolarizing step applied to the *Soma* compartment under neural-wide Ca channel blockade. Application of stimulus and data collection methods were identical to those of the CA1 model.

The PIN model was validated under tonic depolarizations over the range [0.01,0.03] nA at intervals of 0.01 nA as well as 3.5 nA. All depolarizing stimuli were applied to the *Soma* compartment. Stimuli delay times and data collection procedures were identical to those of the CA1 validation experiments.

3.4 Network Bursting Experiments

First, normal juvenile and adult rat CA1 population bursting under $GABA_A$ antagonist was studied. The experimental network is comprised of a 10×10 grid of CA1 pyramidal cells and a 3×3 grid of PIN interneurons. The main axes of all neurons are aligned along the x-axis. Spatial separation of CA1 neurons is 200 ± 40 μm in both the x and y-axis. Spatial separation of PIN interneurons is 450 μm in both the x and y-axis. The PIN neural grid is centered on the CA1 neural grid. Three connectivity types are defined: CA1 recurrent connectivity ratios (PP), CA1 onto PIN excitatory synaptic connectivity ratios (PI), and interneuron onto CA1 inhibitory synaptic connectivity ratios (IP). A connectivity ratio is defined as the number of connections assigned within the simulation divided by the total unique connections possible in the network. All connections are randomly assigned by uniform distribution without regard to spatial constraints.

All experiments incorporate a stimulus profile. Network stimulus is achieved by a single 3.0 nA, 5 ms step depolarization to the *Soma* compartments of n target pyramidal cells. Target pyramidal cells are located at array indices 52-56[2]. Each experimental configuration is identical except for differences in connectivity ratios and the number of externally stimulated cells, n. PI is constant at 0.10 for all experiments. The set of PP values includes 0.01 as well as the range [0.02,0.12] at intervals of 0.02. IP varies over the range [0.05, 0.40] at intervals of 0.05. The number of stimulated pyramidal cells, n, varies over 1,3,4, and 5 for all connectivity ratio permutations.

Second, normal juvenile and adult rat CA3 population bursting under $GABA_A$ antagonist was studied. The experimental network is comprised of a 10×10 grid of CA3 pyramidal cells and a 3×3 grid of PIN interneurons. Anatomical constraints and stimulus profiles are identical to the

[2] Cell indices are defined according to convention of the GENESIS `createmap` command [4]

CA1 network experiments described above. Ranges of connectivity ratios differed from that of CA1 to reflect results reported *in vitro* and via similar CA3 experiments [28, 26, 27]. PI was held fixed at 0.10. The set of PP values includes 0.08 and the range [0.10,0.35] at intervals of 0.05. IP varies over the range [0.20,0.40] at intervals of 0.05.

For all experimental configurations, the following recordings were made. Times denoting occurrence of action potentials were recorded for all pyramidal cells in the network. Resolution of this recording was 0.05 ms. Membrane potential for pyramidal cells receiving external stimulus were sampled at intervals of 0.05 ms.

3.5 Analysis of Bursting Characteristics

No formal mathematical description of bursting has been defined in the literature. However, recordings of the experimental network models were intended to visually resemble electrographic data of synchronous population bursting recorded *in vitro* [19, 22, 17, 20, 21]. An approximate metric, used in the analysis of these models, was devised by visual inspection of *in vitro* recordings [19]. This metric defined bursting as a significant proportion of network neurons firing approximately together one or more times. It is proposed that the proportion of the population involved in a burst, burst frequency, and burst duration are dependent on recurrent connectivity density, mean axonal propagation delay, and neuron kinetics. As is current convention in neural modeling experiments, comparison of simulation results with the results of Shao and Dudek [19] was made visually. This direct visual inspection of cell recordings was supplemented by network-firing activity plots describing the temporal location of all action potentials over all pyramidal cells in the network. While suitable for gross approximations, this method is undesirable in general. The need for automated classification techniques will be described in Chapter 7.

Chapter 4

Validation Results

Understanding the components comprising a biologically-realistic neural network simulation is essential in understanding the network's ability to describe behavior observed *in vitro*. Underlying model assumptions inherently bias the model behavior. Further, the complexity of biologically-realistic neural models makes experimental errors or inaccuracies a common problem. To alleviate concern over model accuracy, due especially to the reimplementation and modification of prior work [28], rigorous validation benchmarking of the CA3, CA1, and PIN neural models is described below.

4.1 CA3 Pyramidal Cells

CA3 pyramidal cells are known to exhibit spontaneous bursting [25]. However, in the context of modeling, spontaneous bursting can be problematic when attempting to understand model behavior. Given original parameter values, the Traub CA3 model exhibits spontaneous bursting [28]. The bursting in this model, however, is largely influenced by membrane resistance parameter. A large value causes current to conduct between compartments rather than across the membrane itself. Trapping current within the model when the simulation is at or near steady-state causes membrane depolarization, spontaneous bursting, and resultant after-hyperpolarization (AHP) as shown in Figure 4.1.

To ensure a stable network at equilibrium, the capacity of spontaneous bursting was removed from the CA3 neuron model through an exhaustive parameter search of membrane resistance. This search yielded 0.5 Ωm^2 as the largest (biologically plausible) membrane resistance ensuring persistent neural stability throughout a simulation run of 3.0 ms. At this level of membrane resistance, the CA3 model will not generate an action potential until it is stimulated directly by externally applied current or via EPSP. This stability facilitates study of the role of recurrent connectivity by permitting a direct trace of action potentials as they propagate throughout the network. The reduction of membrane resistance displayed no significant effects on neuron behavior when stimulated. A suite of external stimulus experiments were applied to the modified model, attempting to mimic those performed by Traub [28]. For the remainder of the discussion, the modified Traub model is referred to as the CA3 model.

To study compartment response to external stimulus, three stimuli scenarios were inflicted on the model: 1) 3.0 nA, 5.0 ms depolarizing step current, injected at the soma, shown in Figure 4.2, 2) 3.0 nA, 5.0 ms depolarizing step current, injected at the soma, coupled with cell-wide blockade of Calcium channels ($g_{Ca,i} = 0.0\ S$), shown in Figure 4.3, and 3) 3.0 nA, 5.0 ms depolarizing current followed immediately by a $-3.0\ nA$, 5.0 ms hyperpolarizing step current, shown in Figure 4.4. All step injections were applied 0.025 sec after simulation start time.

The membrane potential recording of the $Apical_{16}$ compartment in Figure 4.2 provides important evidence as to the nature of dendritic influence on somatic membrane bursting. The massive, slow-acting depolarization in the $Apical_{16}$ compartment, labeled as a calcium-spike by Traub [28], clearly propagates to the soma, as evidenced by the superimposed depolarization profile of the $Apical_{13}$

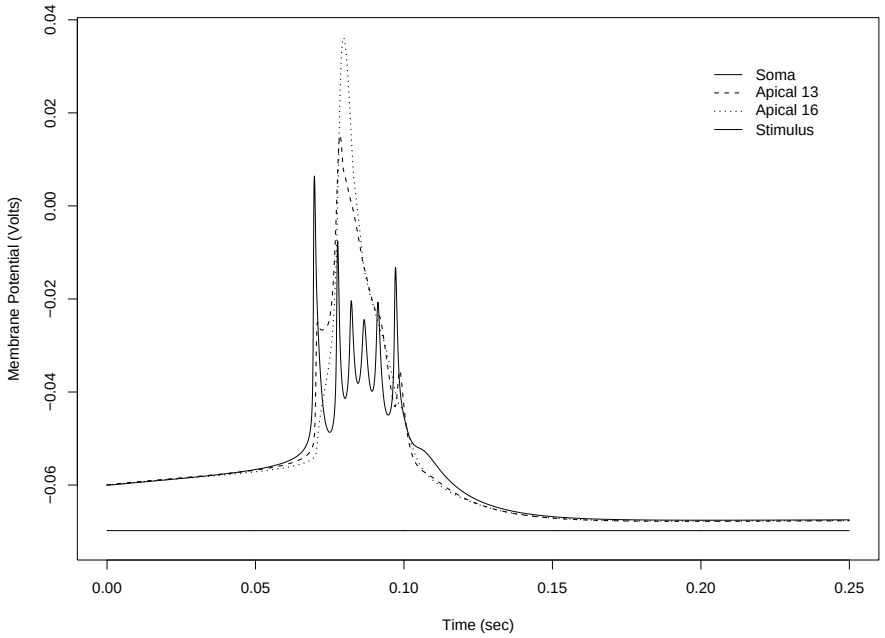

Figure 4.1: Spontaneous bursting exhibited by the Traub CA3 pyramidal cell model without stimulation.

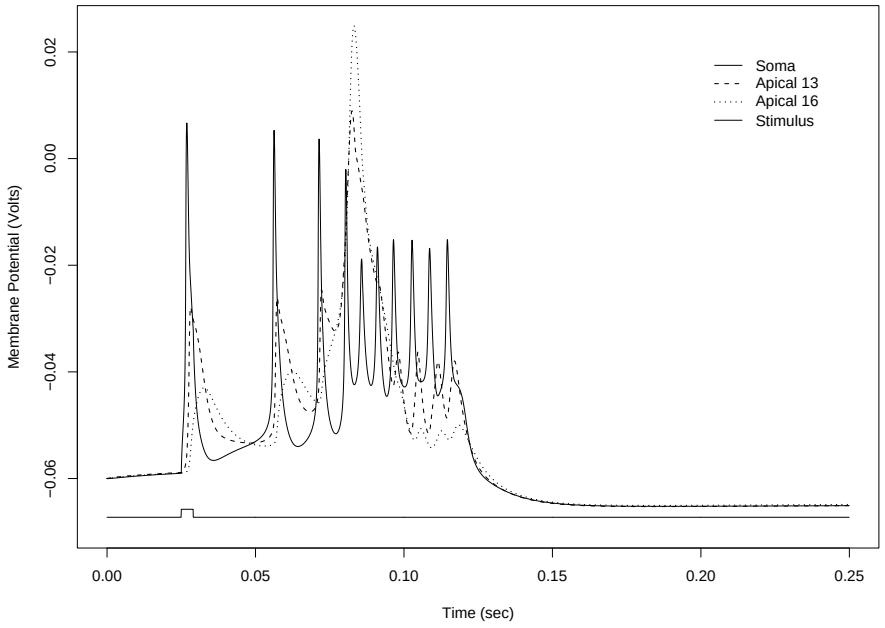

Figure 4.2: Burst response to single depolarizing step applied at the soma.

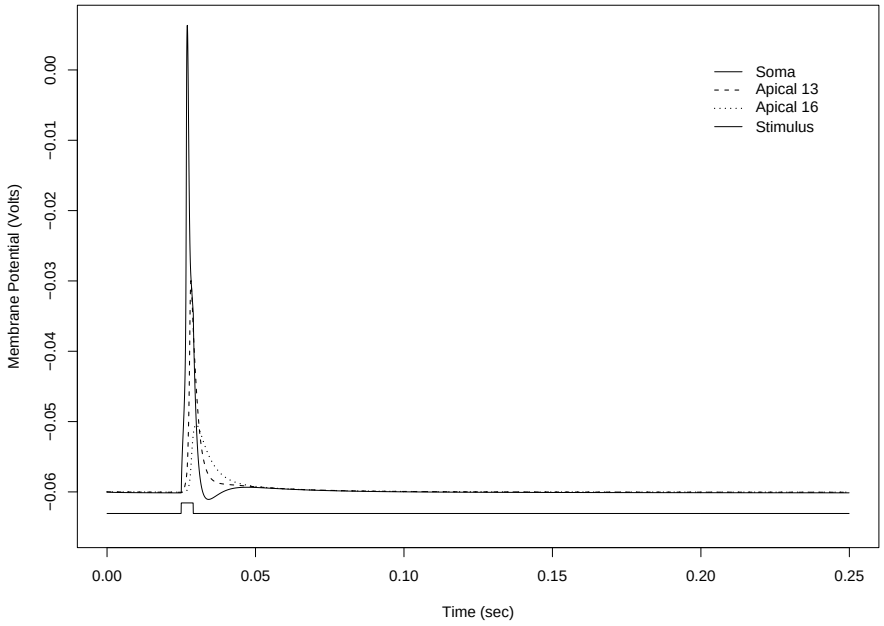

Figure 4.3: Single spike and AHP response to single depolarizing step stimulation of CA3 model under Calcium channel blockade.

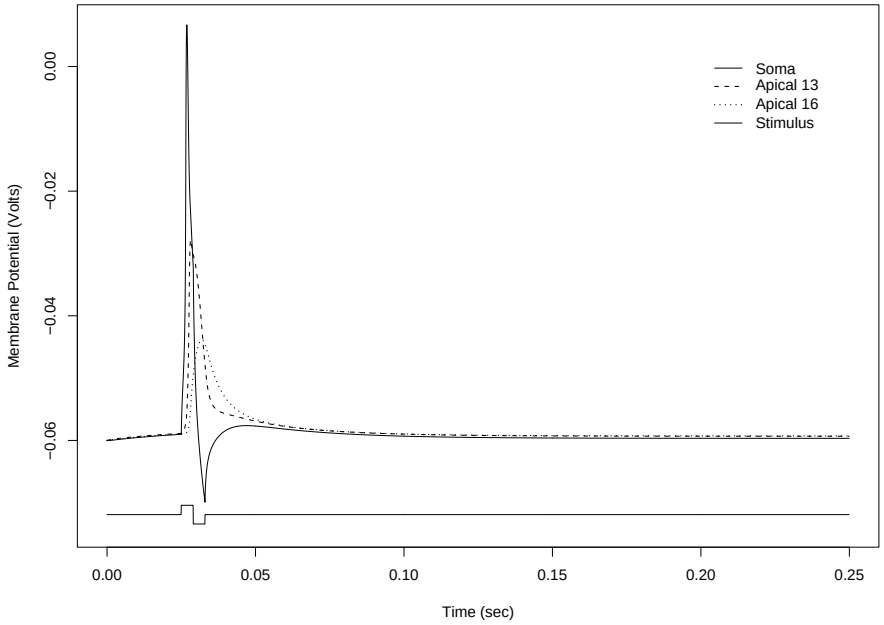

Figure 4.4: Single spike response to depolarizing-hyperpolarizing dual step stimulation applied at the soma.

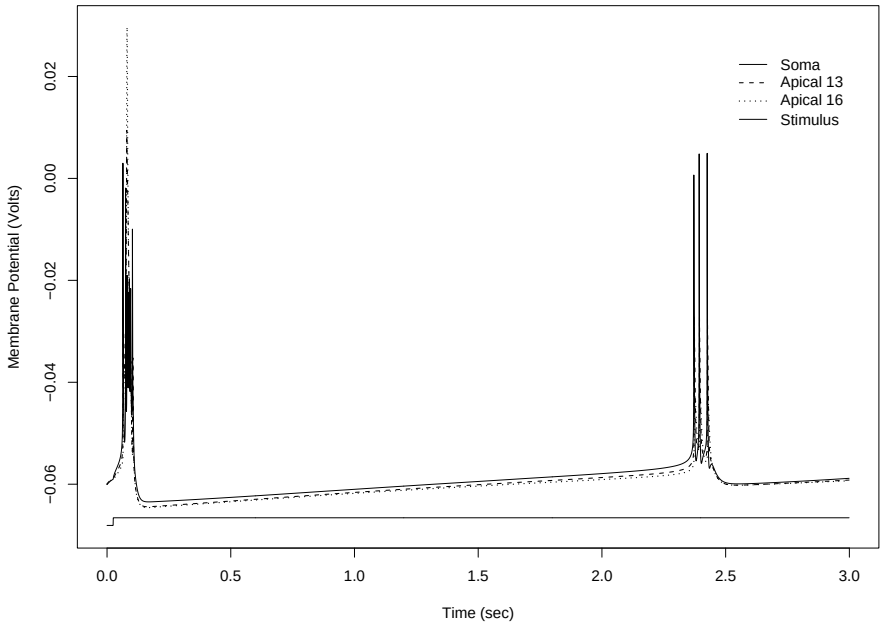

Figure 4.5: Firing mode of CA3 pyramidal cell when 0.1 nA tonic depolarization was applied to the soma.

compartment, which depicts combined membrane properties of these two compartments. This behavior can be strongly supported by the difference in g_{Na} and g_{Ca} channel densities within these compartments. The soma contains high densities of fast acting Na and KDR channels, enabling fast depolarization and recovery behavior. In contrast, dendritic compartments contain relatively high-densities of Ca channels. The interplay of the calcium (and calcium dependent) channels with the calcium concentration shells drives long, powerful depolarizations in the dendrites. These depolarizations invariably excite the soma. This relationship is clearly illustrated when Ca channels are blocked as in Figure 4.3. Without the presence of a dendritic calcium-spike, the soma is unable to develop bursting.

A second, important property of the CA3 is depicted in Figure 4.4. Without a hyperpolarizing step current immediately following the depolarizing step, we would expect to see behavior identical to that of Figure 4.2. However, the immediate hyperpolarization of the soma following depolarization effectively stunts the development of bursting. This is an important property in predicting the effectiveness of fast-acting $GABA_A$ inhibition on CA3 model bursting in a network simulation. A very fast putative interneuron inhibitory feedback response to the initial somatic action potential would subvert CA3 pyramidal cell bursting. This evidence matches well with the high-probability of fast action-potential development in the putative neuron [26].

The CA3 pyramidal cell is also subject to modal firing—consistent firing frequency and depolarization amplitude induced by external stimulation—under varying amounts of tonic depolarization to the soma. Under low tonic depolarizations ($\leq 0.4\ nA$), cell firing exhibits intermittent cell bursting. For larger depolarizations, cell firing is characterized by single spikes with variable recovery adaptation profiles. Figures 4.5-4.8 exhibit a range of these modes. Under the lowest tonic depolarization, 0.1 nA, CA3 pyramidal cells undergo brief bursts distributed at intervals greater than 2.0 *sec*, as is shown in Figure 4.5. Burst separation and intensity decrease as tonic depolarization increases, which is depicted in Figures 4.6, 4.7, and 4.8, sequentially.

The presence of firing modes was originally observed and explained by Traub [28, 26] as a result of the interplay of dendritic calcium-spikes and faster acting systems of channels such as Na and

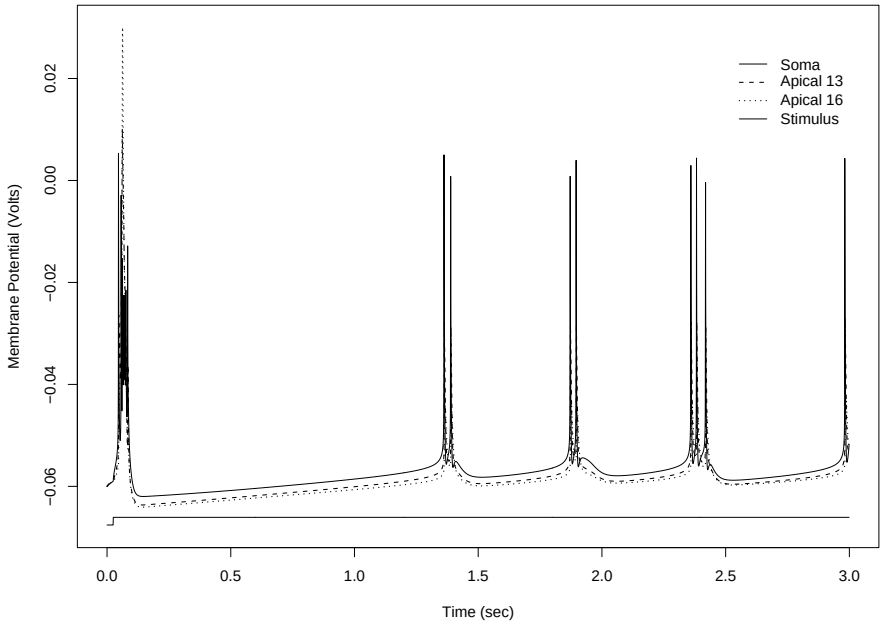

Figure 4.6: Firing mode of CA3 pyramidal cell when 0.2 nA tonic depolarization was applied to the soma.

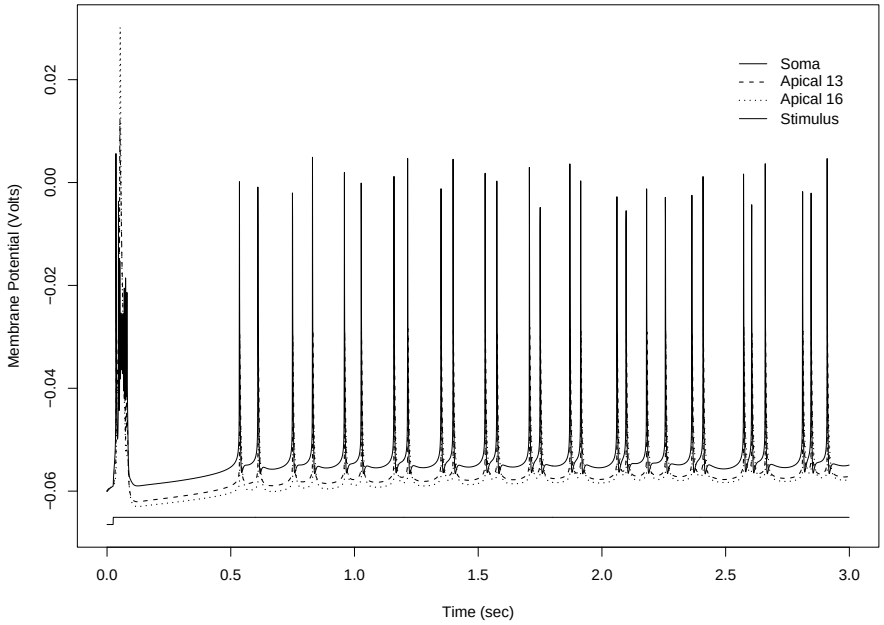

Figure 4.7: Firing mode of CA3 pyramidal cell when 0.4 nA tonic depolarization was applied to the soma.

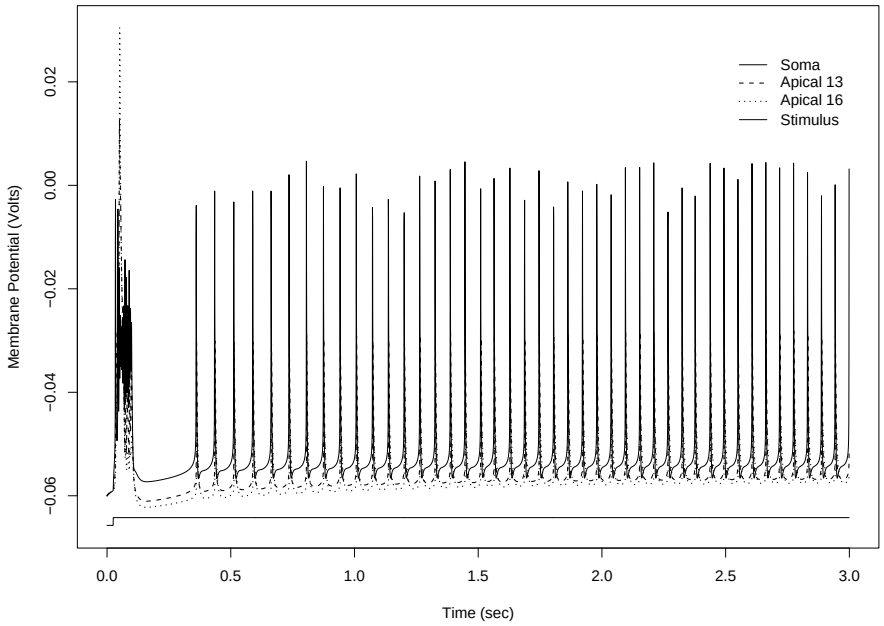

Figure 4.8: Firing mode of CA3 pyramidal cell when 0.5 nA tonic depolarization was applied to the soma.

KDR. Tonic depolarizations propagate to the distal dendritic region and produce calcium currents proportional to somatic depolarization. The size and frequency of calcium-spike development determines the clustering of fast sodium spikes in the soma compartment. Tonic depolarization of compartment $Apical_{16}$ is shown in Figure 4.9. By inspection of the $Apical_{16}$ compartment plot of Figure 4.9, it is clear that large, low-frequency calcium-spikes dictate burst intensity and burst separation in the soma.

4.2 CA1 Pyramidal Cells

Unlike the CA3 pyramidal cell model, the CA1 pyramidal cell model does not contain disproportionately large Ca conductance densities in the apical dendrite. The result of these density differences is significantly less pronounced bursting propensity in the presence of external stimulation. However, in its original configuration, the Traub CA1 pyramidal cell model does exhibit spontaneous firing in the absence of external stimuli. This intrinsic firing property was removed from the model by reducing membrane resistance to 0.7 $\Omega \cdot m^2$. At this resistance level, the model is on the verge of bursting but remains close to rest potential over a reasonably long time-frame ($\geq$ 300 ms). Given a single depolarizing input step current of 3.0 nA for 5.0 $msec$ to the soma compartment, the CA1 pyramidal cell fires a single action potential as shown in Figure 4.10.

As with the CA3 pyramidal cell, the CA1 cell model exhibits some degree of modal firing based on tonic depolarization. As was shown by Traub [28], CA1 model firing modes are highly dependent on the location of stimulation. A 0.25 nA tonic depolarization to the soma and $Apical_{13}$ compartments produces repetitive firing ($\leq$ 60 Hz) with adaptation as shown in Figures 4.11 and 4.12, respectively. Larger tonic depolarizations (1.25 nA) to the distal dendrite induce repetitive firing interleaved with calcium-spike bursts as depicted in Figure 4.14. Unlike results originally reported by Traub [28], the modified CA1 pyramidal cell ($R_M = 0.7\ \Omega \cdot m^2$) generates a full calcium-spike somatic burst when tonic depolarization of the $Apical_{16}$ compartment reaches 0.3 nA, as shown in Figure 4.13. This

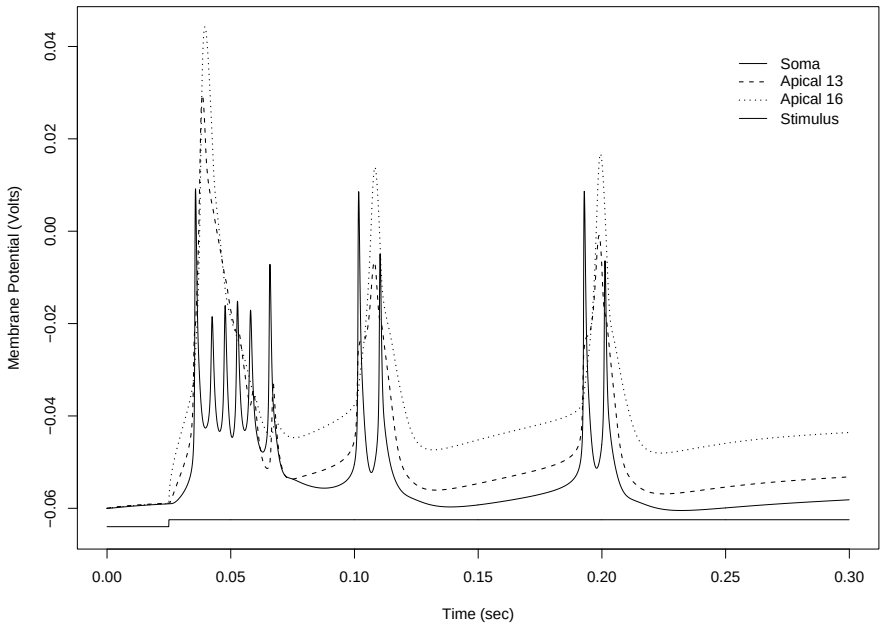

Figure 4.9: Firing mode of CA3 pyramidal cell when 0.5 nA tonic depolarization was applied to compartment $Apical_{16}$.

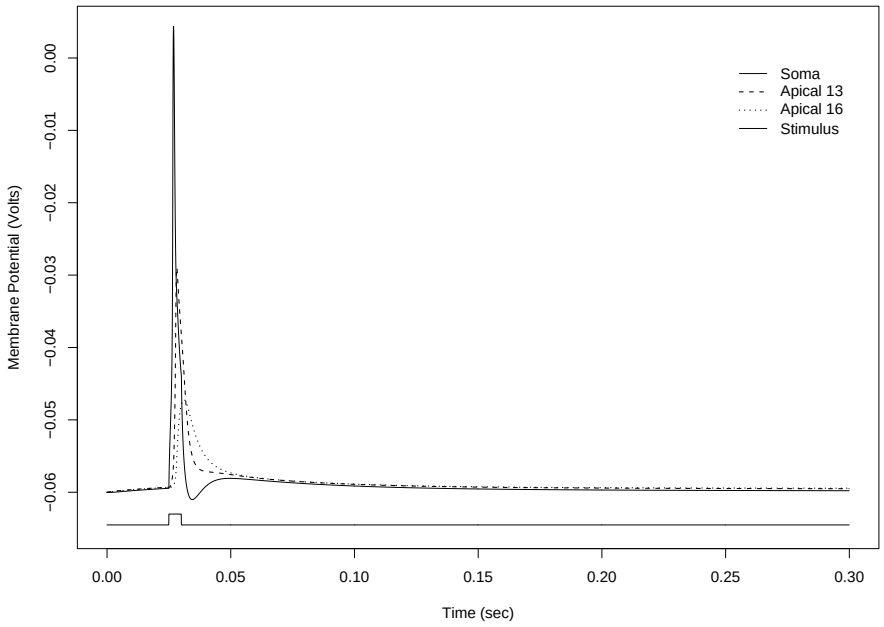

Figure 4.10: CA1 pyramidal cell model response to single depolarizing step current of 3.0 nA for 5.0 $msec$ to the soma compartment.

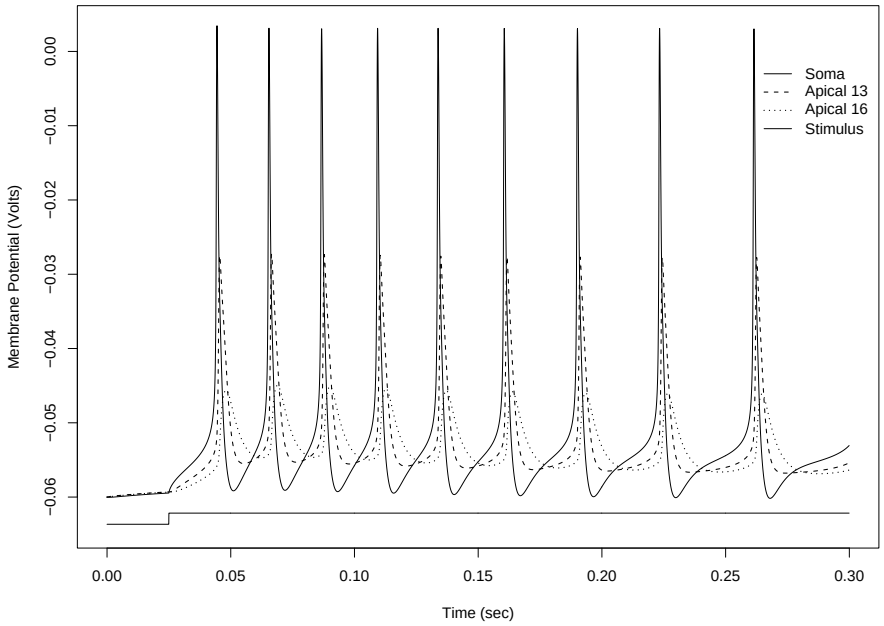

Figure 4.11: CA1 pyramidal cell model response under 0.25 nA tonic depolarization to the *Soma* compartment.

difference is largely attributed to the lower membrane resistance.

From these few simple experiments we have a rich perspective of how a network of recurrently connected CA1 pyramidal cells will behave with respect to CA3. While not predisposed to somatic burst generation, under large tonic depolarization CA1 neurons can and do burst intermittently. CA1 pyramidal cells also display a small degree of modal firing, but the range of modes is more narrow than CA3. However, the nature of the most extreme CA1 bursting intermixed with repetitive firing could easily be reproduced by the superposition of two CA3 pyramidal cells under tonic depolarization of roughly 0.1 nA and 0.5 nA, respectively. Given the weak, slowly developing profile of NMDA conductance during synaptic activation, it is possible to conceive a recurrent connectivity structure in which two neighboring CA3 pyramidal cells have exactly this profile. Moreover, a fully connected network would, as a whole, have many such superposition pairs. This analysis strongly supports the possibility that CA1 and CA3 population bursting could achieve degrees of similarity at appropriate levels of recurrent excitatory connectivity.

4.3 Putative Interneuron

The intended role of a putative interneuron is to distribute inhibition to CA1 and CA3 pyramidal cell networks. Interneurons likely prevent or buffer bursting occurring in these networks, and the accumulation of slow-developing $GABA_B$ inhibitory synaptic currents may play a crucial role in collapsing CA1 and CA3 network bursts over time. Therefore, the PIN model of the putative interneuron has several specific requirements. It must have fast, reliable firing on receipt of an EPSP. It must recover quickly from an AHP to ensure sustained inhibitory capability, and it must be robust against long-term build-up of slow-developing $NMDA$ excitatory synaptic currents, which, in a recurrent network of pyramidal cells, can have substantial additive effects.

The PIN model is inherently unstable. No reasonable variation of membrane parameters was sufficient to eliminate the development of a fast Na spike and subsequent AHP approximately

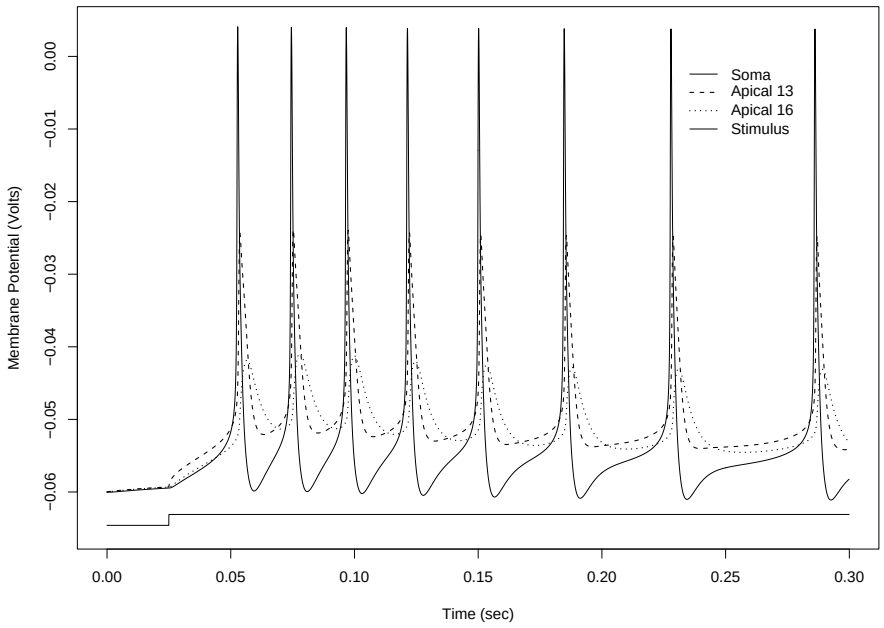

Figure 4.12: CA1 pyramidal cell model response to 0.25 nA tonic depolarization to compartment $Apical_{13}$.

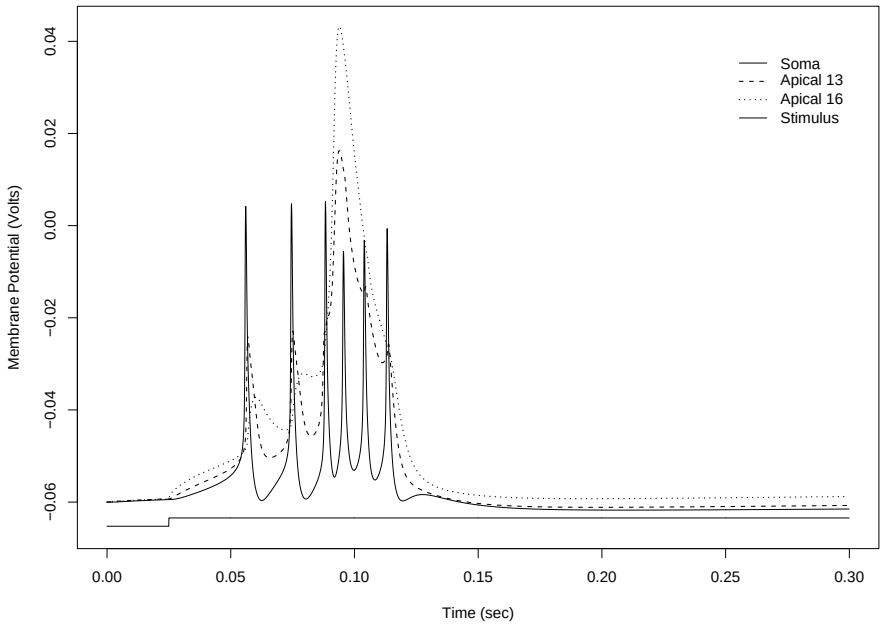

Figure 4.13: CA1 pyramidal cell model response to 0.30 nA tonic depolarization to compartment $Apical_{16}$.

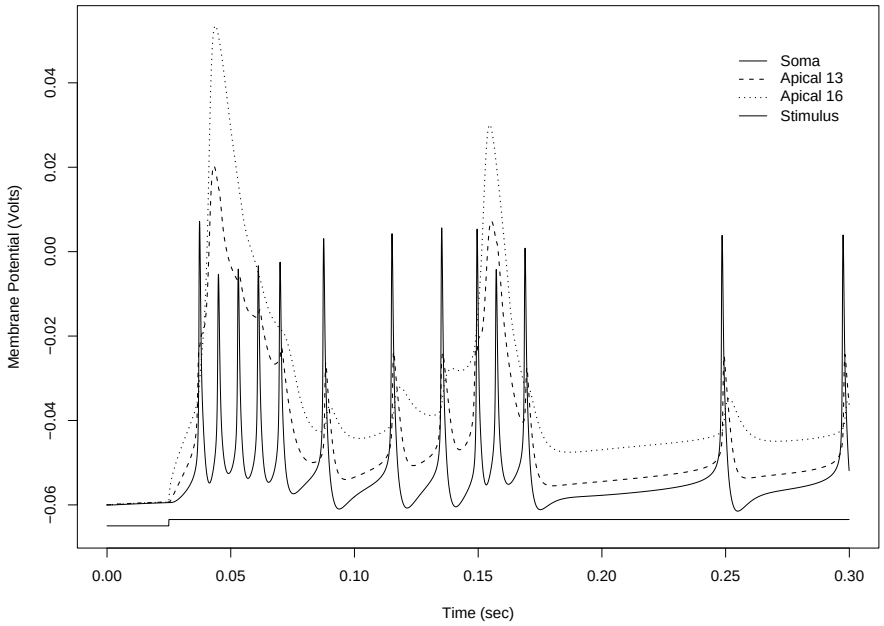

Figure 4.14: CA1 pyramidal cell model response to 1.25 nA tonic depolarization to compartment $Apical_{16}$.

10 $msec$ after start of simulation. This is due, in large part, to the high density of Na channels in dendrite compartment $SD8A$, a necessary component of the PIN model to ensure rapid and successful transfer of an EPSP to the soma. However, the large AHP, a result of delayed rectifier potassium conductance in the dendrite opposing sodium conductance, does not suppress repetitive firing characteristics in the PIN model. Rather, the PIN model exhibits repetitive firing for a wide range of tonic depolarizing currents. The frequency of these currents increases with the magnitude of depolarizing current as shown in Figures 4.15-4.17.

One noticeable feature of PIN model repetitive firing is the decrease in action potential magnitude as frequency increases for large tonic depolarizations ($\geq$ 1.0 nA). A tonic depolarization of 3.5 nA to the soma was found to be the largest depolarization in which PIN model action potentials are super-threshold ($\geq$ 0.0 $Volts$) as is shown in Figure 4.18. This threshold is relevant in that slow-developing, excitatory $NMDA$ synaptic currents could conceivably collapse network inhibition by driving PIN action potentials below threshold. It is proposed that pyramidal cell bursting would continue indefinitely when excitatory synaptic currents induce a collapse of inhibition in this manner. This evidence also reveals the reasoning behind Traub's [28, 26] use of saturation limits on $NMDA$ conductance in network simulations and is invaluable in determining the influence of $NMDA$ conductances in full network simulations.

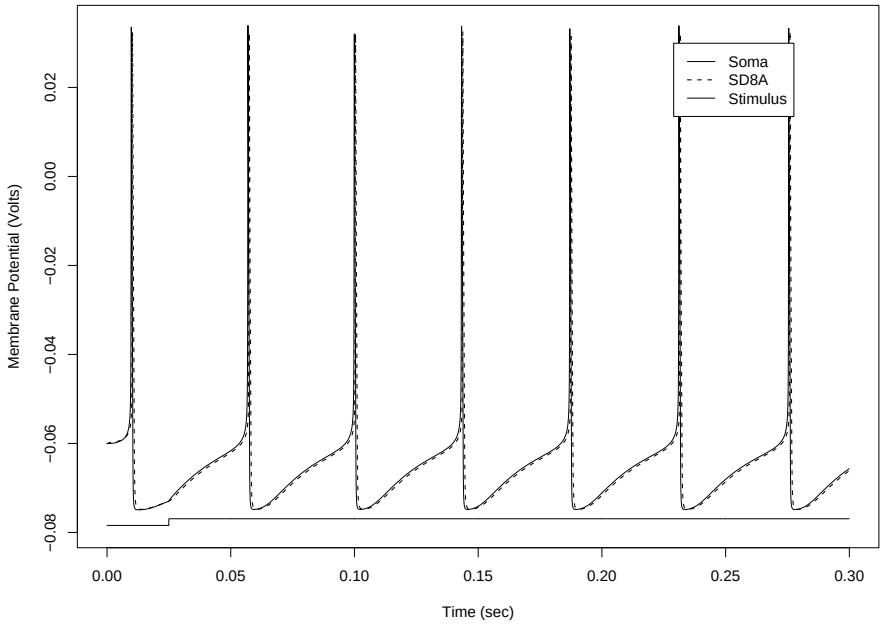

Figure 4.15: Repetitive firing of PIN model at 0.01 nA tonic depolarization of soma compartment.

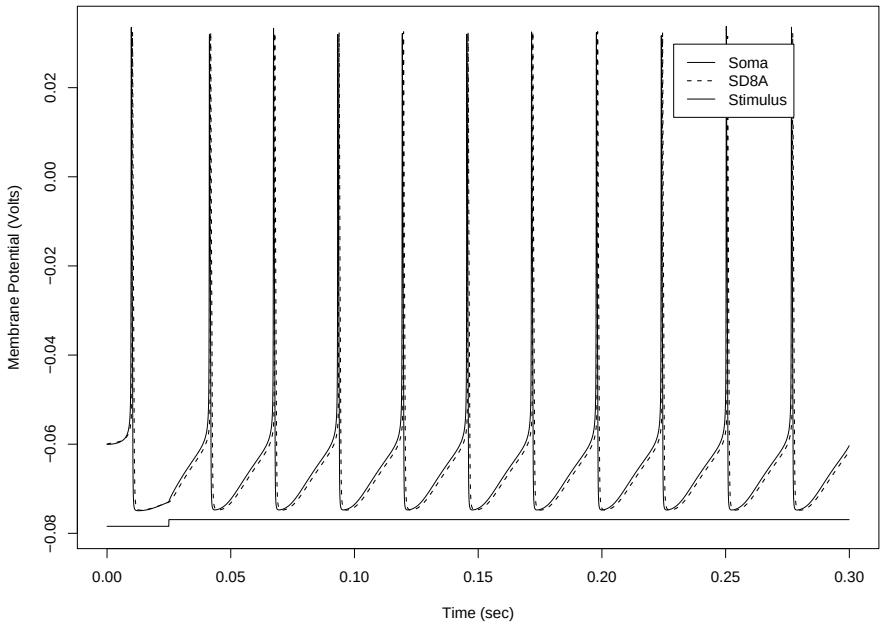

Figure 4.16: Repetitive firing of PIN model at 0.02 nA tonic depolarization of soma compartment.

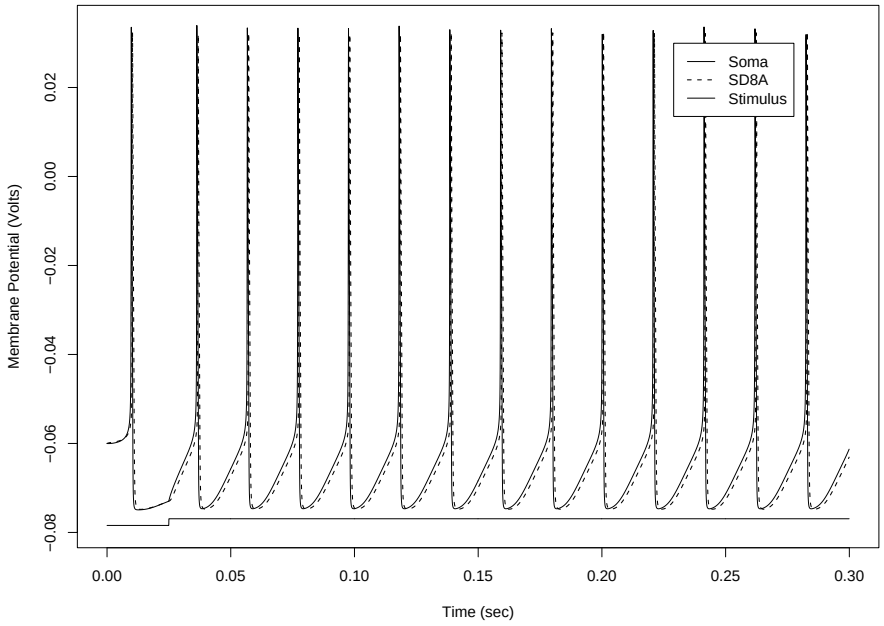

Figure 4.17: Repetitive firing of PIN model at 0.03 nA tonic depolarization of soma compartment.

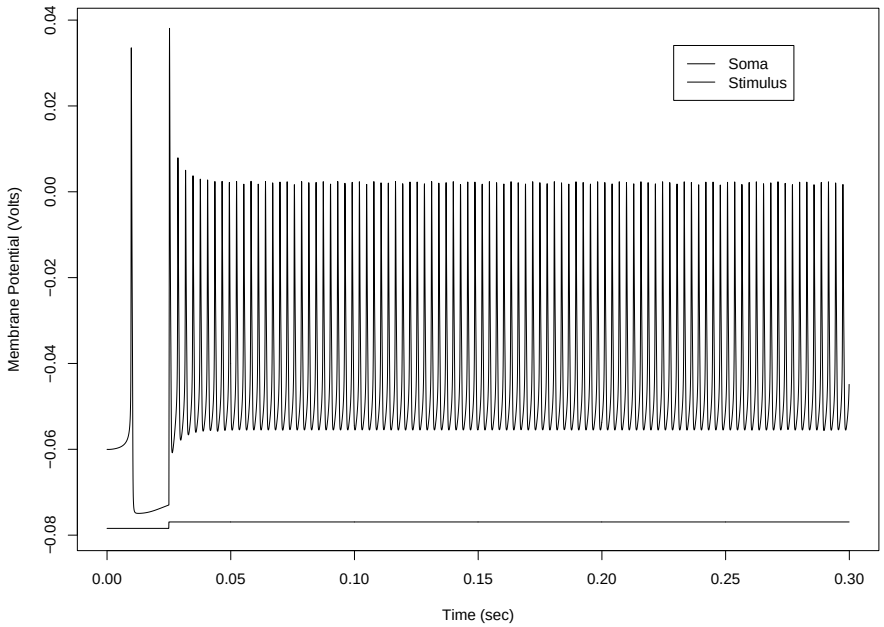

Figure 4.18: Repetitive firing of PIN model at 3.5 nA tonic depolarization of soma compartment.

Chapter 5

Experimental Results

Simulations of computer models described in Section 3 are intended to replicate results reported by Shao and Dudek [19]. Due to the necessity of visual inspection in determining model validity, it is imperative that intracellular and extracellular recordings of *in vitro* hippocampal slices of adult and juvenile CA1 and CA3 regions are presented in combination with simulation results.

Figures 5.1–5.4 depict prototypical recordings used to describe developmental changes influencing CA1 and CA3 population burst characteristics [19][1]. In the remainder of this section, results of simulations mimicking developmental changes will be addressed in detail.

5.1 CA3 Population Bursting Characteristics

The primary focus of this investigation was identification, via visual inspection and comparison, parameter ranges for which the model successfully approximated adult and juvenile CA3 rat hippocampal bursting as inferred from *in vitro* recordings shown in Figures 5.1 and 5.2. CA3 juvenile bursting was best approximated when PP=0.30 and IP was in the range [0.20,0.25]. CA3 adult bursting was best characterized by a CA3 network in which PP=0.20 and IP was in the range [0.25,0.30]. In these configurations, the CA3 networks best depicted the two primary behaviors discriminating *in vitro* adult versus juvenile CA3 behavior—all-or-none bursting and burst duration. The existence of all-or-none bursting, as characterized in Figure 5.5 is a characteristic of the CA3 pyramidal cell network under $GABA_A$ antagonist. In this figure, each point of the plot represents a

[1] Figures marked with † are reproduced with permission of Shao and Dudek [19].

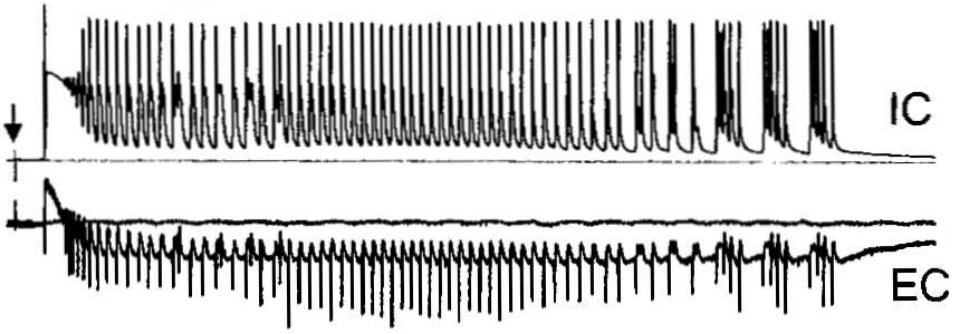

Figure 5.1: Intracellular (IC) and extracellular (EC) recordings of juvenile rat CA3 region *in vitro*. Vertical arrow denotes the application time of external stimulus†.

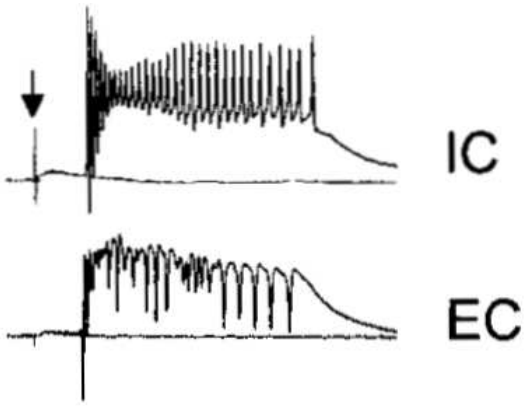

Figure 5.2: Intracellular (IC) and extracellular (EC) recordings of adult rat CA3 region *in vitro*. Vertical arrow denotes the application time of external stimulus[†].

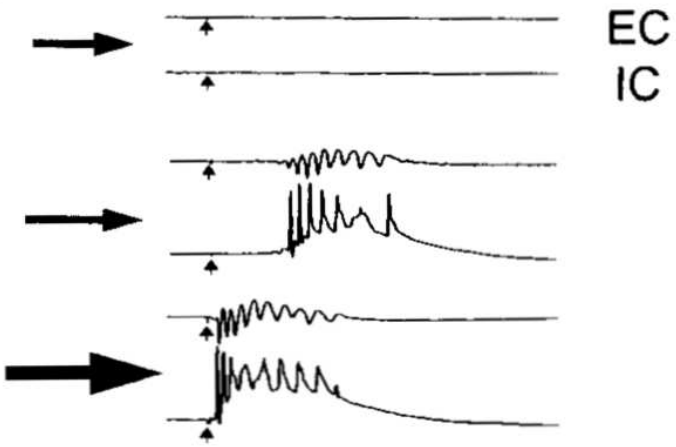

Figure 5.3: Intracellular (IC) and extracellular (EC) recordings of juvenile rat CA1 region *in vitro*. Vertical arrow denotes the application time of external stimulus. Horizontal arrows indicate relative magnitude of external stimulus (i.e. large arrows denote more stimulus than smaller arrows)[†].

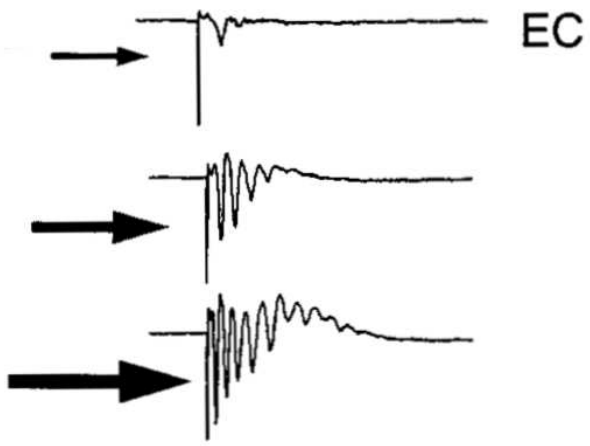

Figure 5.4: Extracellular (EC) recordings of adult rat CA1 region *in vitro*. Vertical arrow denotes the application time of external stimulus. Horizontal arrows indicate relative magnitude of external stimulus (i.e. large arrows denote more stimulus than smaller arrows)†.

single action potential. The y-axis represents each pyramidal cell in the network, plotted irrespective of spatial position. The x-axis denotes time in the simulation.

While the amount and intensity of bursting differs between Figures 5.5(a) and 5.5(b), it is clear that increased stimulation intensity, modeled by increasing the number of cells receiving external stimulus, has little effect on the overall population burst characteristics. Discrimination between Figures 5.5(a) and 5.5(b), adult and juvenile, respectively, is determined by the overall burst focus and intensity. Burst focus is characterized by the time separating the beginning and end of a global network burst, as indicated by the tightly focused vertical bands occurring in Figure 5.5(b) at approximately 40, 80, and 110 ms. Less focused global burst bands are evident in Figure 5.5(a).

Also significant is the model's ability to mimic changes in latent period due to increased stimulation. As external stimulation increases, latent period decreases (i.e. *left* versus *right* within each subfigure) while overall burst intensity and duration remains constant.

Figure 5.5 presents approximations of juvenile and adult CA3 network bursting in which both PP and IP ratios differ. This presentation was made to provide sharp contrast between configurations as well as graphically present the robustness of these developmental models over a number of parameter configurations. Figure 5.6 also compares adult (Figure 5.9(a)) versus juvenile (Figure 5.9(c)), but the comparison is made with inhibitory connectivity held fixed, $IP = 0.25$. The presentation is manipulated to compare network-firing activity alongside a single cell recording of one of the stimulated cells (CA3 cell index=55[2]). Holding inhibition fixed enables a direct comparison of the influence of excitatory recurrent connectivity on population bursts. Clearly, the gross characteristics of Figure 5.5 are maintained.

The single cell recording creates a restricted view of population bursting. While the network-firing activity plot is a more powerful measure of population bursting, this data is difficult or impossible to record *in vitro*. Rather, hippocampal bursting data is often presented as single cell membrane potential recordings or localized extracellular EEG data. The computer model enables side-by-side comparison of a powerful network burst measure with the more familiar *in vitro* sensory method. The intent here is to use model data to understand biological recordings in a more meaningful way.

A striking dissimilarity in Figure 5.6 is the discontinuity between the single cell recording and network-firing activity. Network-firing activity plots (*left*) of Figures 5.9(a) and 5.9(c) clearly show marked differences in burst focus, intensity, and duration. However, the single cell recordings (*right*)

[2]Cell indexing follows convention of the GENESIS `createmap` command.

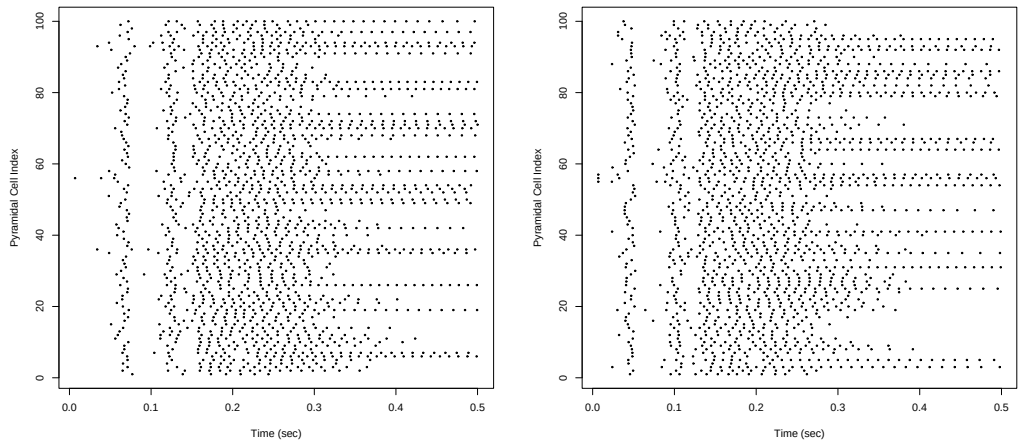

(a) CA3, network, $PP = 0.20$, $IP = 0.30$, single cell stimulation (*left*), 3 stimulation cells (*right*)

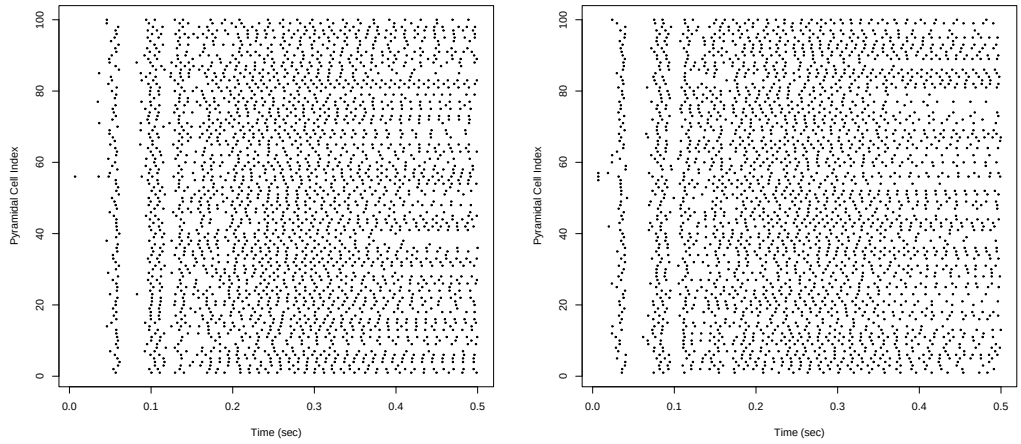

(b) CA3 network, $PP = 0.30$, $IP = 0.20$, single cell stimulation (*left*), 3 stimulation cells (*right*)

Figure 5.5: Example of all-or-none bursting characteristics of CA3 pyramidal cell networks over connectivity ratios identified as plausible bursting upper and lower bounds.

do not differ substantially. The discontinuity found in these data representations may be described by the probability of the recorded cell exhibiting network level effects. If, for instance, the index of the cell recorded in Figure 5.9(c) were incremented by one, the righthand cell recording would depict action potentials and AHPs up to and past the end of simulation. Therefore, we can use network-firing activity data to approximate the probability of bursting through time. For instance, in the adult representation, 21% of cells continue to fire at the end of simulation time (500 ms). In contrast, 37% of pyramidal cells in the juvenile network continue to rhythmically fire at the end of the same time period. In fact, the early phase of bursting is very similar between adult and juvenile networks. The major discriminator characterizing network developmental stage is burst persistence. Juvenile networks have a higher probability of bursting as simulation passes through a threshold time of approximately 250 ms. Less significant differences, such as global burst focus, are only visibly apparent before this threshold.

5.2 CA1 Population Burst Comparison

The CA1 region is known to contain substantially less pyramidal cell recurrent connectivity than that of CA3. Dual-cell recording results [20] estimate mean CA1 recurrent connectivity to fall below 2%. The inherent sparseness of connectivity makes comprehensive estimation of mean CA1 recurrent connectivity prohibitive *in vitro*. Sparse connectivity is problematic due to the influence of small cliques, which can induce bursting variance. Based on best visual inspection of network burst characteristics in the model, CA1 pyramidal cell recurrent connectivity, PP, is estimated to exist on the range 0.02-0.04, or approximately 10-20% of the connectivity observed for a similar sized CA3 network.

However, inhibitory connectivity, IP, plays a significant role in population burst behavior at low recurrent connectivities. Repetitive simulation of the CA1 network over the predicted range of recurrent connectivity produces population behavior that, via visual inspection, requires inhibitory connectivity to fall in the range of 0.25–0.30.

Figure 5.7 depicts simulation results of CA1 network configurations when external stimulus is applied to three neighboring pyramidal cells. Figures 5.7(a), 5.7(b), and 5.7(c) represent CA1 networks having PP connectivity ratios of 0.02, 0.04, and 0.06, respectively. Inhibitory connectivity ratios, IP are 0.25 and 0.30 for lefthand and righthand plots, respectively. The intent of Figure 5.7 is to depict a potential transformation between CA1 adult and juvenile networks within the scope of reasonable recurrent connectivities based on a visual comparison with *in vitro* recordings shown in Figures 5.3 and 5.4. Clearly, Figure 5.7(c) depicts bursting activity far higher than that which is observed *in vitro*. Thus, recurrent connectivity must fall below a ratio, $PP = 0.06$. The differences between $PP = 0.02$ and $PP = 0.04$ approximate behavior reported for CA1 networks in the respective adult and juvenile developmental stages as reported by Shao and Dudek [19]. Exact duplication of *in vitro* data is difficult due to vast differences in membrane potential profiles of individual cells.

The sparseness of connectivity and the influence of inhibition connectivity are evident in Figure 5.7(a). Over multiple simulations (not shown), network-firing activity patterns vary. However, burst intensity, focus, and persistence remained negligible over all redundant simulations. Network-firing activity for recurrent connectivity levels below 0.02 is negligible. The prevailing behavior of CA1 networks at connectivities below 0.06 may be characterized by the absence of synchronous population bursting. Some limited, localized bursting is evident when recurrent connectivity reaches 0.06. For recurrent connectivity greater than 0.06, population bursting emerges. This phenomena will be revisited in the next section.

Having motivated the range of connectivity for the transformation between juvenile and adult CA1 networks to fall between 0.02 and 0.04, analysis turned to the study of burst characteristics in response to variable external stimulus. Figures 5.8 and 5.9 depict CA1 network firing for connectivities of $PP = 0.02$ and $PP = 0.04$, respectively. Within each figure, the amount of external stimulus increases from the top pair of plots to the bottom pair. Increasing external stimulus is modeled by the number of pyramidal cells recruited in application of the externally applied step current. Further, the left and right columns of these figures contrast the effects of graded bursting

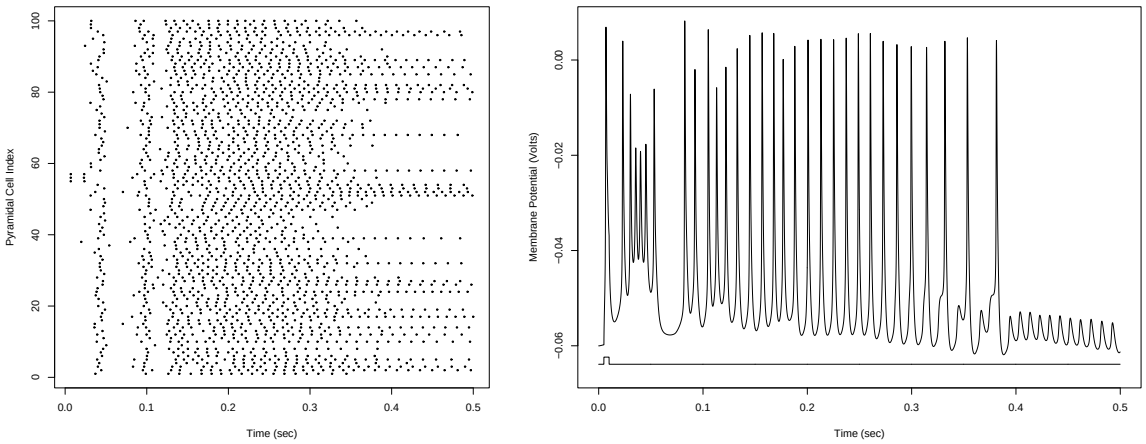

(a) CA3 adult network-firing activity and stimulated cell recordings.

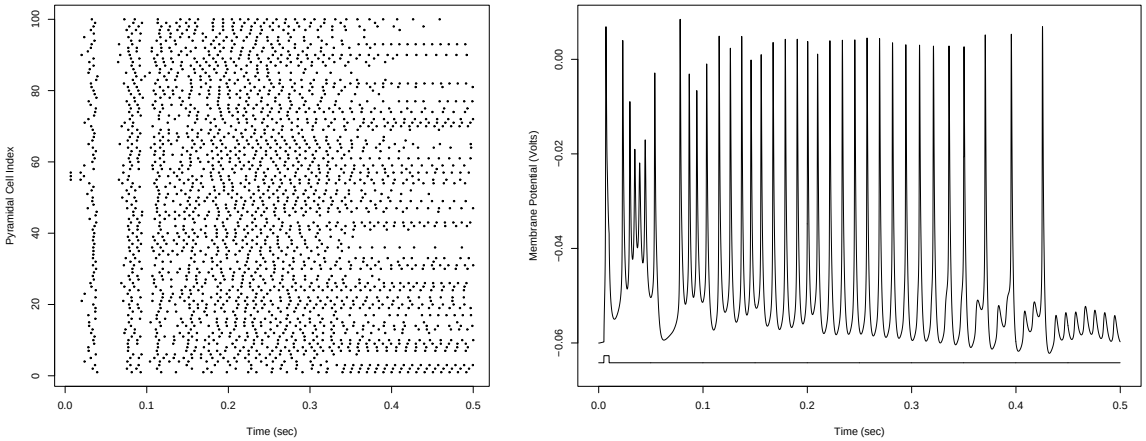

(b) CA3 juvenile network-firing activity and stimulated cell recordings.

Figure 5.6: Example of all-or-none bursting for CA3 adult and juvenile networks.

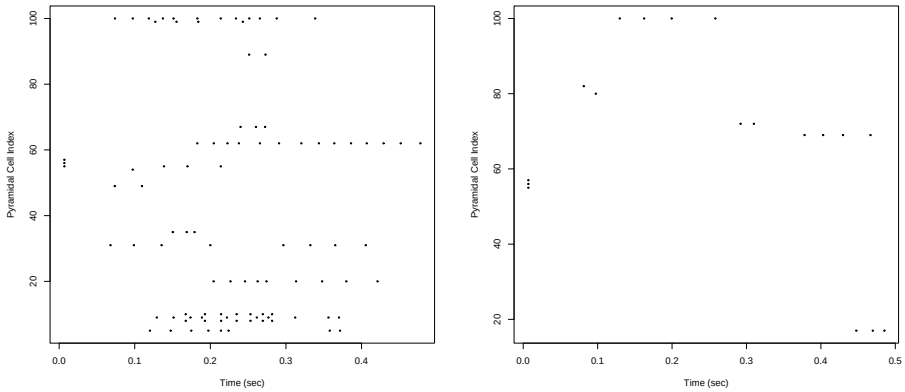

(a) $PP = 0.02$, 3 stimulation sites.

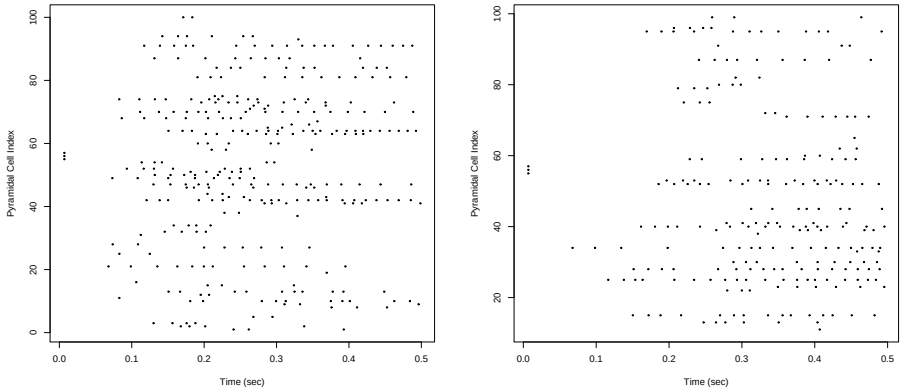

(b) $PP = 0.04$, 3 stimulation sites.

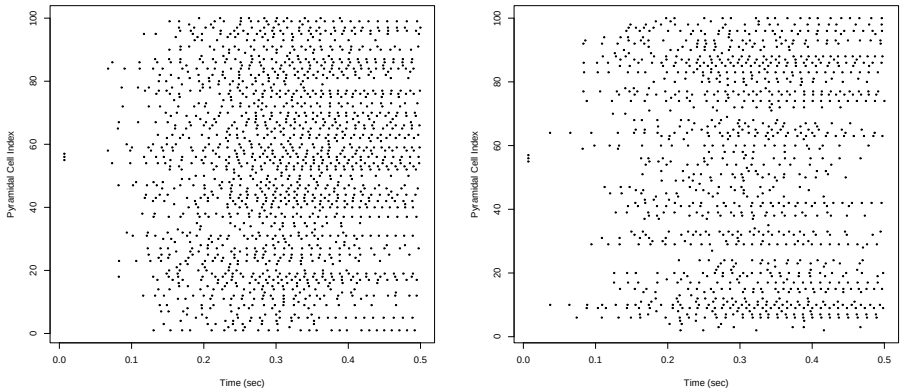

(c) $PP = 0.06$, 3 stimulation sites.

Figure 5.7: Example transformation of adult to juvenile CA1 burst characteristics. $IP = 0.25$ (*left*) $IP = 0.30$ (*right*).

in differing climates of inhibition. The left column of Figures 5.8 and 5.9 describes increasing external stimulus for networks in which $IP = 0.25$. In the right columns, IP was fixed to be 0.30. Redundant simulations over identical parameters produced wide variance in the results. Bursting activity generally increased as the number of stimulated neurons increased from one to three. As the number of stimulated neurons increased from three to five, however, changes in burst activity varied widely. No discrimination, based on a visual interpretation of bursting, could be discerned.

5.3 Contrasting the CA1 and CA3 regions via Modeling

A key benefit of computer modeling is the capability to simulate networks with neural connectivities outside ranges observable *in vitro*. The normal rat CA3 hippocampal region is known to display much greater excitability than the normal CA1 region under $GABA_A$ antagonist. However, it is crucial to understand the role connectivity plays in this characterization. Results of validation experiments on CA1 and CA3 neurons in Section 4 indicate that CA1 neural models are as likely or more likely to fire action potentials at equivalent levels of tonic depolarization. Therefore, in the presence of slow-developing EPSPs ($NMDA$) we would suspect CA1 networks to achieve significant network bursting given a sufficient recurrent connectivity density. An interesting result then, would be a direct comparison of CA1 and CA3 networks composed with identical connectivity ratios. When CA1 and CA3 networks are compared in identical climates, where the recurrent connectivity artificially resides above the realistic CA1 connectivity upper bound and below the connectivity lower bound of CA3, the underlying hyper-excitability of the CA1 region relative to CA3 emerges. This striking realization is presented in Figure 5.10. In both CA1 and CA3 networks, external stimulus was applied to a single pyramidal cell. Connectivity ratios for both networks were defined as follows: $PP = 0.08$, $PI = 0.10$, and $IP = 0.20$.

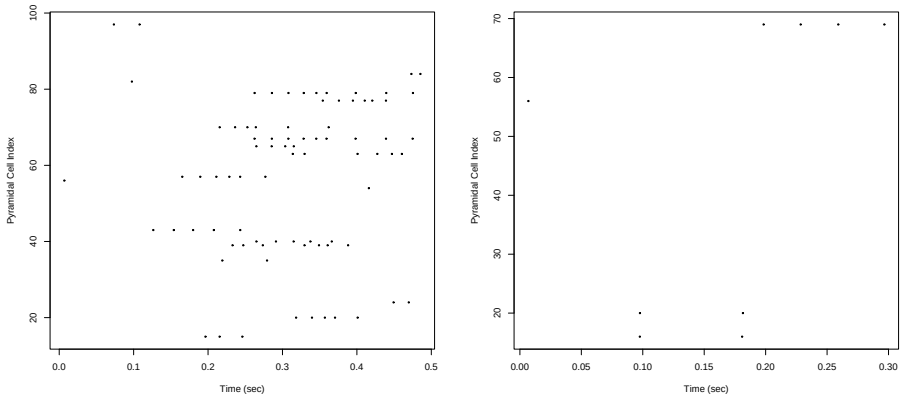

(a) 1 stimulation site

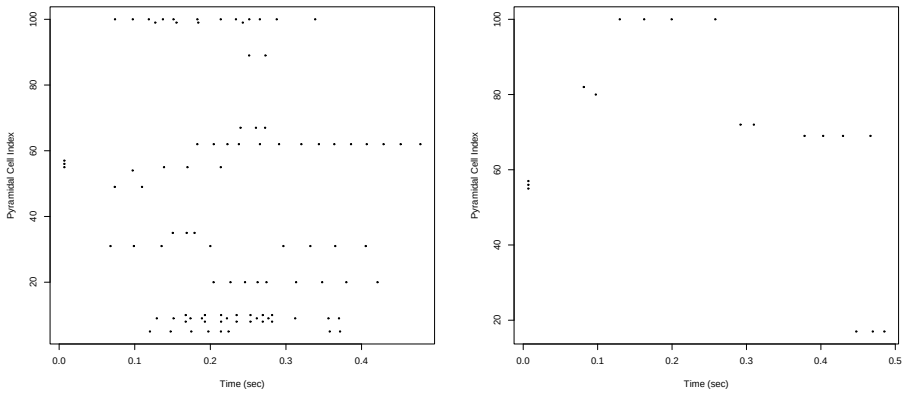

(b) 3 stimulation sites

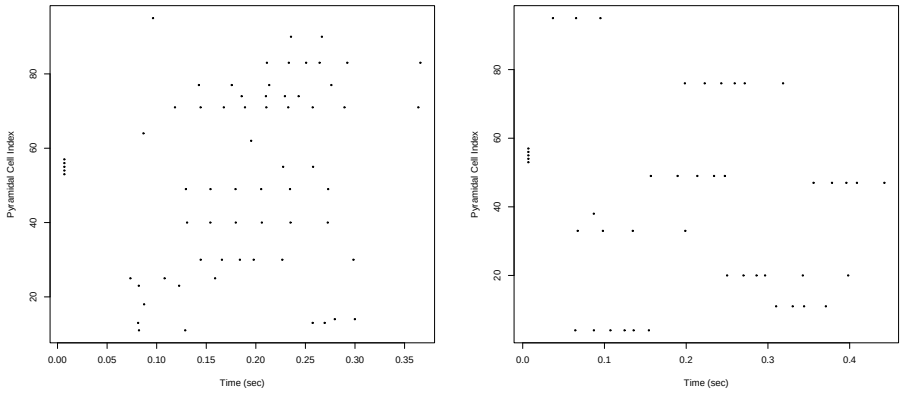

(c) 5 stimulation sites

Figure 5.8: Graded population bursting of CA1 networks, $PP = 0.02$, $PI = 0.10$, $IP = 0.25$ (*left*) $IP = 0.30$ (*right*)

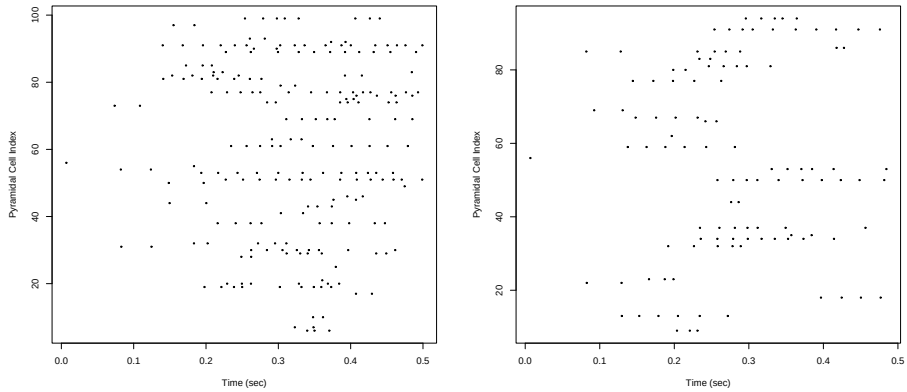

(a) 1 stimulation site

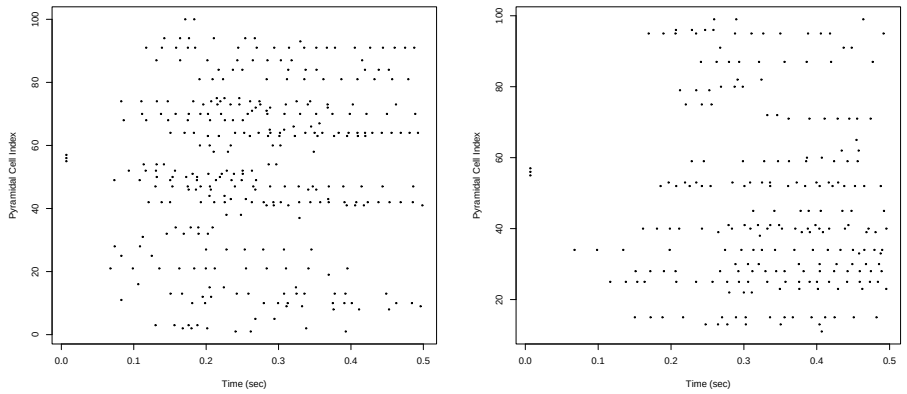

(b) 3 stimulation sites

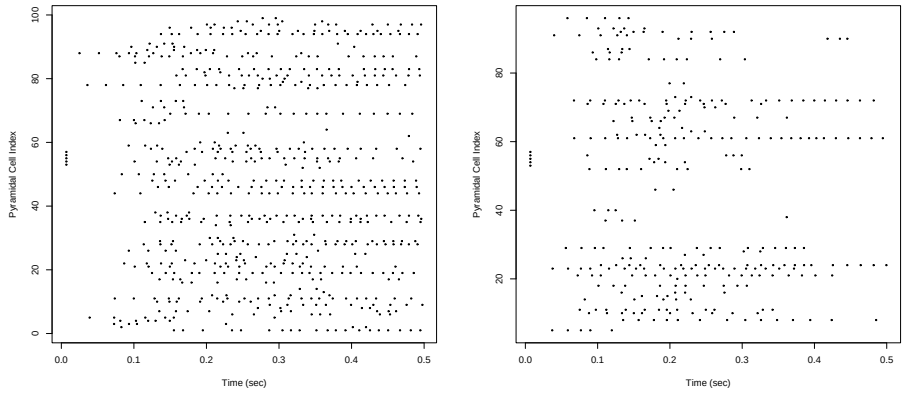

(c) 5 stimulation sites

Figure 5.9: Graded population bursting of CA1 networks, $PP = 0.04$, $PI = 0.10$. $IP = 0.25$ (*left*) $IP = 0.30$ (*right*)

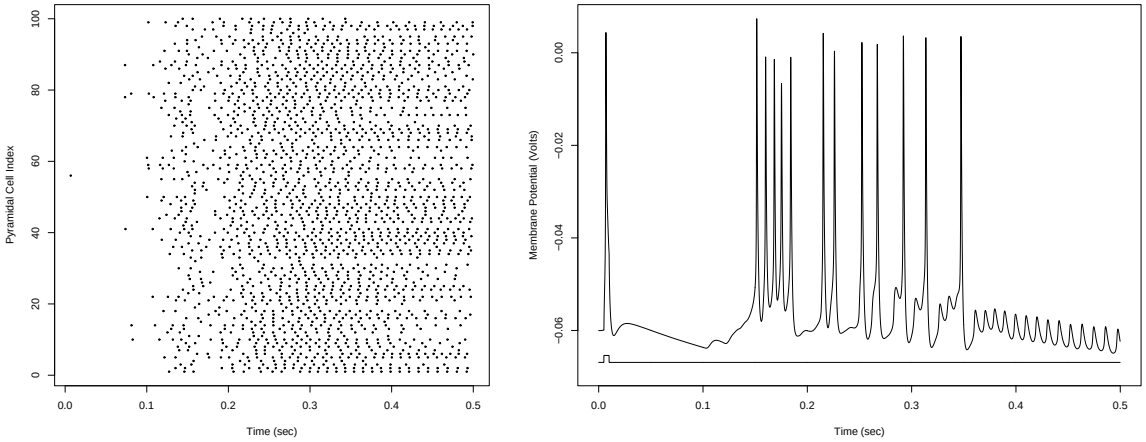

(a) CA1 network

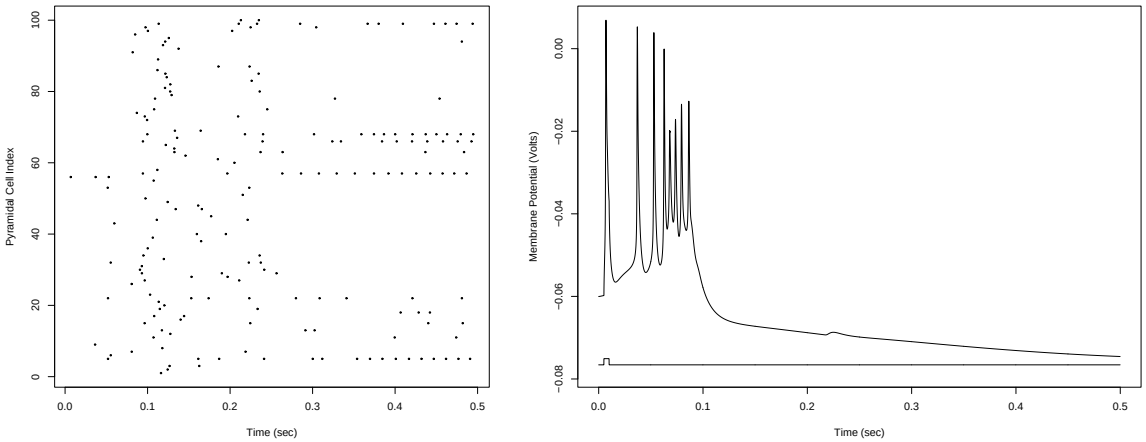

(b) CA3 network

Figure 5.10: Comparison of CA1 and CA3 networks when $PP = 0.08$, $PI = 0.10$, $IP = 0.20$. Single neuron stimulation. Action potential histogram (*left*) and single cell recording (*right*) of externally stimulated cell.

Chapter 6

Discussion

I have presented approximate connectivity distributions that describe changes in network burst properties observed to occur in the Sprague-Dawley rat CA1 and CA3 hippocampal regions at both *juvenile* and *adult* developmental stages. These connectivity approximations were motivated by computer simulations of small-scale CA1 and CA3 network models. Approximations and behavior depicted, however, closely map to values and behavior recorded *in vitro* [19]. The data used for classification included action potential histograms and single cell membrane potential recordings generated via computer model. Classification of behavior was performed by visual inspection of resultant data and comparison of data across model configurations.

In addition to modeling developmental changes in the CA1 and CA3 reasons, the experiments uncovered the dominance of CA1 bursting propensity over that of the CA3 region when connectivity levels are held constant between regions. This result was both counterintuitive and enlightening. The propensity of CA1 bursting at recurrent connectivity ratios greater than 0.08 may actually influence the inherent sparse connectivity of these region.

While not reported in results, models of CA3 networks in which recurrent connectivity ratios were greater than 0.30 produced substantially higher levels of global burst focus, intensity, and persistence. These models may be significant evidence for the existence of the role of synaptic reorganization and MFS in epileptiform bursting exhibited by the rat kainate-model.

Chapter 7

Future Work

As mentioned in the previous section, a recurrent connectivity model of network bursting provides substantial evidence to the MFS model of epileptiform bursting in the CA3 region. Additionally, this model may extend to the dentate gyrus. Similar experimentation as described in this paper, with the intent of studying epileptiform bursting rather than developmental changes, should be performed on recurrent models of dentate gyrus granule cells. Combined with results reported herein, the MFS model of epileptiform bursting would be substantial.

Scaling of the results for the small-scale models reported here is an important step in understanding robustness. Recurrent connectivity ratios defined herein were used to generate discrete connectivity counts. These discrete counts may be applied to larger models. A primary concern in scaling is the effect of axonal propagation delay. Larger networks clearly must incorporate biologically motivated connectivity distributions to reflect distance as a physical constraint of connectivity observed *in vitro*. A probability of connectivity, linearly decreasing with distance is proposed as in initial step in modeling local connectivity over a large network of (≥ 1000) pyramidal cells.

With regards to parameter estimation, the techniques and methods utilized in this research are inadequate. Hand-tuning of model parameters and visual inspection of simulation data are inherently tedious, error-prone, and subjective. Modern artificial intelligence methods should be applied to the entire procedure of model construction, parameter optimization, data mining, and data analysis. However, as stated previously, no mathematically well-defined definition of network bursting exists. An immediate step beyond the current research is the determination of a mathematically well-defined network burst metric. Given a reliable metric, classification of simulation results could be achieved. Given a reliable classification capability vast machine learning resources and techniques would then become available to build, simulate, and study biologically realistic neural models. Automation of the process will leverage computational power, and enhance the speed and accuracy of modeling research.

REFERENCES

[1] T.L. Babb, W.R. Kupfer, J.K. Pretorius, P.H. Crandall, and M.F. Levesque. Synaptic reorganization by mossy fibers in human epileptic fascia dentata. *Neuroscience*, 42:351–363, 1991.

[2] J.S. Bains, J.M. Longacher, and K.J. Staley. Reciprocal interactions between CA3 network activity and strength of recurrent collateral synapses. *Neuroscience*, 2:720–726, 1999.

[3] Y. Ben-Ari. Limbic seizure and brain damage produced by kainic acid: mechanisms and relevance to human temporal lobe epilepsy. *Neuroscience*, 14:375–404, 1985.

[4] J.M. Bower and D. Beeman. *The Book of Genesis*. Springer-Verlag, New York, NY, 1997.

[5] P.S. Buckmaster and F.E Dudek. In vivo intracellular analysis of granule cell axon reorganization in epileptic rats. *J. Neurophysiology*, 81:712–721, 1999.

[6] S. Clark and W. Wilson. Mechanisms of epileptogenesis and the expression of epileptiform activity. In *The Treatment of Epilepsy: Principles and Practice*, pages 53–81, Baltimore, MD, 1996. Williams and Wilkins.

[7] D.R. Fish and M.C. Walker. Pathology of epilepsy. In *Epilepsy Comprehensive Review and Case Discussions*, pages 13–21, London, 2001. Martin Duntz Ltd.

[8] M. Hines. A program for simulation of nerve equations with branching geometries. *Int. J. Biomed. Comput.*, 24:55–68, 1989.

[9] A.L. Hodgkin and A.F. Huxley. The components of membrane conductance in the giant axon of loligo. *J. Neurophysiology*, 116:473–496, 1952.

[10] A.L. Hodgkin and A.F. Huxley. Currents carried by sodium and potassium ions through the membrane of the giant axon of loligo. *J. Neurophysiology*, 116:449–472, 1952.

[11] A.L. Hodgkin and A.F. Huxley. The dual effect of membrane potential on sodium conductance in the giant axon of loligo. *J. Neurophysiology*, 116:497–506, 1952.

[12] A.L. Hodgkin and A.F. Huxley. A quantitative description of membrane current and its application to conduction and excitation in nerve. *J. Neurophysiology*, 117:500–544, 1952.

[13] E.R. Kandel, J.H. Schwartz, and T.M. Jessell. *Principles of Neural Science*. Appleton and Lange, East Norwalk, CT, 1991.

[14] W. Lytton, K.M. Hellman, and T.P. Sutula. Computer models of hippocampal circuit changes of the kindling model of epilepsy. *Artificial Intelligence in Medicine*, 13:81–97, 1998.

[15] M.V. Mascagni and A.S. Sherman. Numerical methods for neuronal modeling. In *Methods of Neuronal Modeling: From Ions To Networks*, pages 569–606, Cambridge, MA, 1998. MIT Press.

[16] C.L. Meier and F.E. Dudek. Spontaneous and stimulation-induced synchronized burst afterdischarges in the isolated CA1 of kainate-treated rats. volume 76, pages 2231–2239, 1996.

[17] P.R. Patrylo and F.E. Dudek. Physiological unmasking of new glutamatergic pathways in the dentate gyrus of hippocampal slices from kainate-induced epileptic rats. *J. Neurophysiology*, 79:418–429, 1998.

[18] P. Pinsky and J. Rinzel. Intrinsic and network rhythmogenesis in a reduced traub model for ca3 neurons. *Comp. Neuroscience*, 1:39–60, 1994.

[19] L. Shao and F.E. Dudek. Evidence for a decline in recurrent excitation and seizure susceptibility in the hippcampal CA3 and CA1 subregions during maturation. *Submitted to J. Neurophysiology*, October, 2003.

[20] B.N. Smith and F.E. Dudek. Short and long term changes in CA1 network excitability after kainate treatment in rats. *J. Neurophysiology*, 85:1–9, 2001.

[21] B.N. Smith and F.E. Dudek. Network interactions mediated by new excitatory connections between CA1 pyramidal cells in rats with kainate-induced epilepsy. *J. Neurophysiology*, 87:1655–1658, 2002.

[22] G. Sperk. Kainic acid seizures in the rat. *Prog. Neourbiol.*, 42:91–96, 1994.

[23] K.J. Staley, J.S. Bains, A. Yee, J. Hellier, and J.M. Longacher. Statistical model relating CA3 burst probability to recovery from burst-induced depression at recurrent collateral synapses. *J. Neurophysiology*, 86:2736–2747, 2001.

[24] K.J. Staley, M. Longacher, J.S. Bains, and A. Yee. Presynaptic modulation of CA3 network activity. *Nature*, 1:201–209, 1998.

[25] R.D. Traub and J.G.R. Jefferys. Mechanisms responsible for epilepsy in hippocampal slices predispose the brain to collective oscillations. In *Neural Modeling and Neural Networks*, pages 111–127, Oxford, 1994. Pergamon Press.

[26] R.D. Traub, J.G.R. Jefferys, R. Miles, M.A. Whittington, and K. Toth. A branching dendritic model of a rodent CA3 pyramidal neurone. *J. Physiology*, 481:79–95, 1994.

[27] R.D. Traub and R. Miles. Pyramidal cell-to-inhibitory cell spike transduction explicable by active dendritic conductances in inhibitory cell. *J. Comp. Neuroscience*, 2:291–298, 1995.

[28] R.D. Traub, R.K.S. Wong, R. Miles, and H. Michelson. A model of a CA3 hippocampal pyramidal neuron incorporating voltage-clamp data on intrinsic conductances. *J. Neurophysiology*, 66:635–650, 1991.

[29] J. Wuarin and F.E. Dudek. Electrographic seizures and new recurrent excitatory circuits in the dentate gyrus of hippocampal slices from kainate-treated epileptic rats. *Neuroscience*, 16:4438–4448, 1996.

Appendix A

GENESIS Overview

GENESIS (GEnereal NEural SImulation System) is an object-oriented scripting environment designed specifically for the simulation of neural models. Script code is parsed and converted into compiled C++ objects making the execution of GENESIS scripts very fast. High-level language features of GENESIS enable quick development time. This section is a brief overview of how a GENESIS simulation is created as well as a listing of key GENESIS object features used in this research.

Script object are stored in a directory hierarchy very similar to the Linux operating system. Directories in GENESIS are termed elements. Top-level objects reside in the / element. A top-level object's name is used in a directory path format to access lower-level objects. The element path `/soma/Ca` is an example of an access path, where the `soma` object exists at the top-level and the `Ca` object resides within that object. The canonical GENESIS script begins by defining a set of prototype elements that exist outside the simulation hierarchy in a separate element path denoted `/library`. Objects are created by a script titled `protodefs.g` and stored in `/library`. Once prototype objects are created, scripts of any name with the `*.g` suffix create copies of the prototype objects in some meaningful way. Simulation objects are connected together via messages, using the `addmsg <source> <dest> <msg type> <msg field>` paradigm.

Copies of objects are changed to build specific object constructs by calling the `setfield <object> <param> <value>` command. The `<object>` field denotes the path from top-level where the object resides, the `<param>` field is a specific private quantity contained within the object, and the `<value>` field is the location at which a user-defined quantity, intent to become the `<param>` field's value, is positioned.

Once a suitable set of objects have been created, initialized, and connected in some meaningful way the `reset` and `step <numsteps>` must be called. The `reset` command allows built-in GENESIS error-checking features to determine if the simulation code in syntactically, and to some extent, electrotonically correct. The `step` command tells the GENESIS environment how many simulation time steps to advance–it is up to the developer to infer what a timestep means by the type of units used to initialize objects. Three important points should be remembered when programming in the GENESIS script language. First, scoping is dynamic. Second, all object copies are deep copies. Third, message passing arguments are compiled down to pointers in C++ code, thus, message passing is extremely fast during execution.

A.1 Object Reference

A complete specification of the GENESIS language is available online at `www.genesis-sim.org/GENESIS` and an excellent tutorial is available [4]. The following section is a small description of object types and common commands used in this research.

1. `Ca_conc`: Calcium concentration shell object.
2. `create`: GENESIS script constructor call

3. `readcell`: Constructor call used to build an entire neural compartment model based on a `*.p` configuration file.

4. `setclock`: Sets the simulation clock. GENESIS allows for up to 16 unique simulation clocks to be used.

5. `setfield`: Accessor method call of a GENESIS object.

6. `symcompartment`: Cylindrical compartment object that stores anatomical shape and passive membrane properties. Cylinders are linked end-to-end and may contain shell and channel object links to simulate realistic neural membrane patches.

7. `synchan`: Synaptic channel object.

8. `tabchannel`: Gated ion channel object based on a predefined look-up table.

9. `createmap`: Constructor call used to generate an abstract array container of GENESIS objects. This array object is generally used for anatomically grouping neurons.

Appendix B

Neuroscience Principles

The neuron is the backbone of information processing in the brain. However, by itself a single neuron has limited processing capability. The brain contains uncountable variations of neural networks, systems of interconnected neurons, to satisfy a wide range of processing needs. To understand how neural networks serve as information processors, however, one must understand the anatomical and physiological architecture of a simple neuron first. Only then can the role of complex interconnectivity be understood as a cohesive functional unit.

B.1 The Neuron

From an information processing perspective, the purpose of the neuron is to receive, process, and retransmit signals. Signals, in this context, are disruptions in the membrane potential of the neuron. A neuron, for reasons to be discussed later, maintains an electrical potential across its membrane of approximately -60 to -70 mV. Because the equilibrium potential is negative, the neuron is said to be hyperpolarized with reference to the extracellular space. Signals generally take the form of depolarization, positive change, of the membrane potential. Depolarizing changes propagate across the neural membrane such that a depolarization at a dendritic branch will propagate to the axon hillock. Membrane depolarizations have a second property, they are additive. For example, a depolarization of 15 mV occurring adjacent to a depolarization of 20 mV causes the locations between to have a depolarization of some linear combination of these values, greater than either value individually (≥ 20). Neural anatomy is configured to take advantage of membrane potential changes to convey and process information. A generalized neuron is depicted in Figure B.1 to aide in the discussion of anatomical functionality.

At a high-level, neural anatomy may be decomposed into five sections: the dendritic tree, the soma, the axon hillock, the axon proper, and axonal branches. Functionally, however, the neuron has three sections: reception and integration, decision, and retransmission. Information is received in the dendritic tree via synaptic connections. Details of the synapse will be provided later, but initially, we can think of synaptic connections as physical locations where inbound signals are collected by the neuron. All signals propagate to the axon hillock where their effects are summed. If the summed depolarizations, via the additive property, achieve a fixed threshold depolarization, an action potential occurs. An action potential is defined as an all-or-none, massive depolarization of the neural membrane. The axon and axonal branches serve the purpose of transmitting the action potential over long distances and to many different locations. To aide understanding, a graphic depicting a generalized neuron in provided in Figure B.1.

With this high-level description in place, the underlying information processing functionality of the neuron is available for study. The highly complex branching structure of the dendritic tree serves to collect numerous incoming signals from many different neurons. Due to passive propagation and additive properties of the membrane depolarizations occurring at synaptic connections, the dendritic tree can be viewed as a giant antennae that collects signals. As signals propagate down the branch

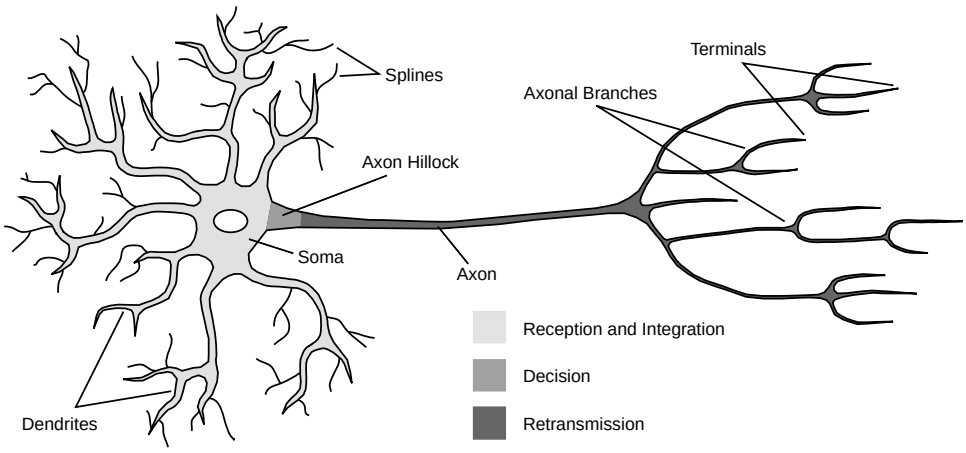

Figure B.1: Generalized depiction of a neuron.

structure they are summed at intersections. The entire dendritic tree, may be referred to as the signal collection component.

As signals propagate down the dendritic tree, they eventually reach a single terminus, the axon hillock. All signals are summed at this location. Therefore, the axon hillock may be viewed as the signal integration component. However, the axon hillock does not just passively sum incident signals. This section of the neural membrane contains a high density of voltage-gated ion channels. These channels have the effect of magnifying membrane depolarizations should the passive sum of the depolarization achieve some value above a fixed threshold value, which varies from neuron to neuron. In a very basic way, the combined effects of the voltage-gated ion channels in the axon hillock form a binary switch. When summed membrane depolarization is below some value, the switch remains off, and passive propagation continues through the axon hillock and down the axon. However, if the summed depolarization reaching the axon hillock achieves a value greater than (i.e. less negative than) the threshold, the the switch is turned on. Turning on the switch is equivalent to generating an action potential, a massive depolarization, of approximately 100 mV.

The axon and axonal branches have the duty of transmitting action potentials to various locations in a neural network. The axon, via its natural myelin sheath insulation, is capable of transmitting action potentials over large distances, quickly, and with little loss of potential. Some axons can be as long a one meter and achieve signal transmission velocities of 1 m/s. Axonal branches may carry the action potential to several thousand other neurons.

B.2 The Synapse

The synapse is the location of transfer between neurons. Formally, the synapse is empty space separating the axonal terminal of the presynaptic neuron with the dendrite of the postsynaptic terminal. Unlike signal propagation within a neuron, signal transmission between neurons occurs via chemical signaling. At a high-level, the process is comprised of discrete, sequential steps. First, an action potential must propagate to the axonal terminal of the presynaptic neuron. The depolarization of the membrane caused by the action potential causes vesicles containing neurotransmitters to bind to the membrane of the presynpatic axonal terminal. These vesicles then rupture, releasing neurotransmitter into the empty space separating the presynaptic and postsynaptic neurons, properly called the synaptic cleft. Neurotransmitters diffuse across the synaptic cleft and bind to neurotransmitter specific receptors located on the dendritic membrane of the postsynaptic neuron. These receptors in turn cause ion-channels to open, allowing diffusion of ions across the postsynaptic neural membrane, depolarizing the membrane. Propagation of the signal then proceeds passively as described previously. Neurotransmitter is absorbed by surrounding support cells, specifically astrocytes. Vesicles

are filled and repaired in the neuron nucleus. Slow transport processes are responsible for moving vesicles containing neurotransmitter from the nucleus to the axonal branches as well as returning ruptured vesicles for repair and refilling.

The type of neurotransmitter released by the presynaptic neuron governs the function of the synaptic connection. Synaptic connections are classified in two ways, excitatory and inhibitory. Excitatory synapses cause depolarization of the postsynaptic neuron. Inhibitory synapses hyperpolarize the postsynpatic neuron, or secondarily, block the function of nearby excitatory synapses. The type of neurotransmitter and the functionality of the postsynaptic receptor govern this classification. While hundreds of neurotransmitters have been discovered, the four most significant types are defined below:

- **AMPA** (*alpha-amino-3-hydroxyl-5-methyl-isoxazole-4-proprionate*), fast excitatory
- **NMDA** (*N-methyl-D-aspartate*), slow excitatory
- **GABA$_\mathbf{A}$** (*gamma-aminobutyric acid, A-type*), fast inhibitory
- **GABA$_\mathbf{B}$** (*gamma-aminobutyric acid, B-type*), slow inhibitory

The fast and slow specifications above concern the rate at which depolarization or hyperpolarization is induced in the postsynaptic neuron. Fast synapses may cause potential change in $1-3\ ms$. Slow synapses may effect potential changes over $20-40\ ms$. Speed of influence and excitatory or inhibitory behavior differ widely among known neurotransmitters. For greater detail readers are directed to Kandel, Scwhartz, and Jessell [13].

B.3 Neural Networks

The process of signal collection, integration, and retransmission within a single neuron has been shown to be equivalent to a non-linear function. A collection of neurons, given certain assumptions, can then be shown to be mathematically equivalent to a linear combination of non-linear functions. Theoretically, any function may be approximated via a linear combination of non-linear functions, given enough non-linear functional elements exist.

While the exact role of the entire brain has not been determined, the functionality of subsections has been determined experimentally. Details of these analysis are beyond the scope of this paper.

Appendix C

Neural Modeling Principles

C.1 Membrane Potential

Neurons convey information via electrical and chemical signals. Neural membrane potential is the mechanism by which this signal information is conveyed. As discussed previously, an overly simplified neuron is a lipid-bilayer compartment of intra-cellular fluid, cytoplasm, bathed in extracellular fluid. Both intra-cellular and extracellular fluid types contain concentrations of various ions, particles carrying net positive charge (cations) and net negative charge (anions). For the purpose of explanation, we will propose that these fluid contain significant concentrations of only two ionic species, potassium and sodium. The extracellular fluid contains a relatively greater concentration of sodium ions, Na^+, and the cytoplasm contains a relatively greater concentration of potassium, K^+, ions. Both fluid types contain mixtures of these two ionic species.

This system, a barrier separating solutions of differing concentrations of ionic species, is the definition of a battery. We know intuitively that batteries are sources of electrical potential and current. Given this perspective, we may define membrane properties by means of electromagnetic. Ohms Law is the relationship governing these basic relationships and is defined by the following equation.

$$V = I \cdot R \tag{C.1}$$

where V denotes potential (Volts), I denotes current (Amps), and R denotes resistance (Ohms). Potential is directly proportional to current and resistance. Thus, potential may be thought of as the driving force of current. Current is the movement of charged particles through a circuit. Resistance represents the opposition of current in a circuit.

It is well known that all neural membranes possess a multitude of ion-selective channels that facilitate the diffusion of ions across the membrane barrier. Unique channel types vary by the thousands if not millions. However, for simplicity we consider only passive, non-gated channels selective to one of the two species available, Na^+ or K^+. These channels allow electro-chemical forces to drive ionic transfer across the barrier via diffusion. The existence of ionic flow across the membrane defines what is called ionic current, I_{ion}. As with electrical circuits, ionic current and membrane potential behave according to Ohms Law.

With Ohms Law behind us, we can now investigate well-understood theory to explain the relationship between ionic concentrations, membrane potential, and ionic current. However, we must abstract further for clarity. Consider temporarily that the neural membrane is impermeable to Na^+. This is equivalent to stating that the membrane's resistance to Na^+ ion diffusion is infinitely large, which by Ohms law would make Na^+ potential equal to zero. Therefore, only K^+ ions may transfer across the membrane and the electro-chemical potential across the membrane, at equilibrium, may be described by the Nernst Equation:

$$E_K = \frac{RT}{ZF} \ln \frac{[K^+]_o}{[K^+]_i} \tag{C.2}$$

where R is the ideal gas constant, T is temperature, F is the Faraday constant, and Z is the effective valence of K^+. Thus, if we consider equilibrium conditions to have constant temperature then $\frac{RT}{ZF}$ is constant and equilibrium depends only on the natural logarithm of the quotient of K^+ ionic concentration outside and inside the membrane, respectively. Further, when extracellular and intra-cellular K^+ concentrations are equal, it is obvious that $E_K = 0\ mV$.

Detailed experimental measurements have determined $E_K = -75\ mV$. This result demands one further explanation. Neurons normally carry net negative charge within the cell and net positive charge externally. Canonically, notation describing membrane potential as positive or negative assumes that negative potential indicates excess intra-cellular negative charge, although it should be obvious that the opposite convention would also be appropriate.

For completeness, the Nernst Equation describing potential generated by separation of extracellular and intra-cellular Na^+ ions given that the membrane is impermeable to K^+ ions, follows:

$$E_{Na} = \frac{RT}{ZF} \ln \frac{[Na^+]_o}{[Na^+]_i} \tag{C.3}$$

E_{Na} has been determined experimentally to be approximately $+55\ mV$. Again, note the relative nature of this number, indicating that a significant net positive charge exists extracellularly. The realistic neural membrane is more complex. A normal neuron contains passive channels permeable to both K^+ and Na^+ ions. Fortunately, equilibrium potential for the influence of multi-species, non-gated channels is well-understood and described by the Goldman Equation as follows:

$$V_m = \frac{RT}{F} \ln \frac{p_K[K^+]_o + p_{Na}[Na^+]_o}{p_K[K^+]_i + p_{Na}[Na^+]_i} \tag{C.4}$$

where p_K and p_{Na} are membrane permeabilities to K^+ and Na^+ ions, respectively. These values may be thought of as the relative densities of open-gated, ion specific channels present in the membrane for each ionic species. Thus, the Goldman Equation can be thought of as a more generalized version of the Nernst Equation. In fact, if the permeability of one species is set to zero, then the Goldman Equation reduces to the Nernst equation for the remaining species.

A question should arise in your mind at this point. Both the Nernst Equation and Goldman Equation describe the equilibrium potential achieved when concentrations of ionic species are maintained on opposite sides of the membrane. However, we also state that non-gated channels exist that allow diffusion of ionic species across the barrier. If this is the case, then any equilibrium condition cannot be maintained as ions flow from high concentration to low concentration. This diffusion of ions down the concentration gradient will drive the membrane potential to $0\ mV$. How is this possible?

Thankfully, the answer is well understood. All neurons contain a metabolic process called the $Na^+ - K^+$ pump. The $Na^+ - K^+$ pump functions to maintain net negative charge in the intracellular space. This is achieved by a chemical process in which 3 Na^+ ions are transported out of the neuron and 2 K^+ ions are transported into the neuron with the hydrolysis of ATP [13] as the result. Thus, equilibrium concentrations in the extracellular and intra-cellular space are maintained. The imbalance of Na^+ to K^+ transfer during the $Na^+ - K^+$ pump cycle has an additional effect. The unequal 3-2 transfer of cations across the membrane forces additional K^+ ions to diffuse across the membrane into the neuron, forming an net ionic current at equilibrium. The current is often called *leak*.

Experimental measurements have shown that neural membranes in which only non-gated Na^+ and K^+ channels account for ionic diffusion have an equilibrium membrane potential,V_m, of approximately -60 to $-70\ mV$. Canonically, the membrane potential in this configuration is defined as the resting potential denoted, E_{rest}. Given this very negative membrane potential it should be clear from the Goldman Equation that the permeability of K^+ channels dominates that of Na^+ channels when at resting equilibrium.

Another important topic of discussion, one that will be raised many times later in this paper, is the understanding of how the rest potentials relate to ionic current. The E_{Na}, E_K, and E_{rest} potentials may be thought of as theoretical batteries driving ionic currents in and out of the neuron

as stated by Ohms Law. At steady-state, E_{rest} acts as the combined driving force of ionic current, which as was discussed, is dominated by relatively high passive K^+ diffusion across the membrane (high K^+ ion permeability). E_{rest} is slightly depolarized from E_K due to the effects of membrane permeability of Na^+ ions as described by the Goldman Equation.

C.2 Passive Membrane Properties

The brain's purpose is to generate, disseminate, and process signals. We define a signal to be a unit of information. In the case of biological neurons, the physical manifestations of the signal are magnitude and rate of change of membrane potential. In the previous section we learned how membrane potential is defined at steady-state, physiologically based, and how Ohms Law determines the relationships between potential, current, and resistance. This section developed understanding of how the magnitude of membrane potential is determined. The rate of change of potential, with respect to time or space, requires further investigation.

Before we move onto these topics, however, we must discuss another electromagnetic concept that is critically important in neural function, capacitance. Capacitance is the ability to store and release charge. Capacitance relates to potential by the following equations:

$$V = Q/C$$

$$\Delta\ V = \Delta\ Q/C$$

where C is capacitance, V is potential, Δ V is change in potential, Q is charge, and Δ Q is the change in charge stored on the capacitor. To understand the role of capacitance in membrane potential rate of change, let us assume that the membrane is a capacitor in addition to being a resistor as described in the previous section. Given this, the charge carried by membrane current, I_m, must be decomposed into two pieces, ionic current, I_i, and capacitive current, I_c, related by the following equation:

$$I_m = I_i + I_c$$

The ionic current, as described previously, is defined by the net ionic diffusion across the membrane and behaves as described by Ohms Law. Capacitive current, however, has the property of adding and removing charge stored on the membrane itself. An outward capacitive current would then be described by the addition of cations to the intra-cellular surface of the membrane and removal of an equal number of cations from the extracellular surface. This is analogous to storage of current that flows in the opposite direction. The remainder of the section describes how the membrane's capacitive properties influence potential rates of change through both time and space.

C.2.1 Membrane Potential Temporal Rate of Change

The equation governing the rate of change of membrane potential with respect to time is given below:

$$\Delta V_m(t) = I_m R(1 - e^{-t/\tau})$$

where t denotes time and τ denotes the membrane time constant, a dimensionless quantity defined as the time required for the membrane potential to reach 63% of the value induced by a disruption of membrane current. An obvious observation follows. Given a command current, a step of current applied externally to the membrane, the membrane potential response behaves as a bounded non-linear function of time governed by the membrane time constant. Related time signatures exist within the ionic and capacitive components of the membrane current as shown in Figure C.1.

The lower plot of Figure C.1 depicts a step of command current as well as the ionic, I_i, and capacitive, I_c, components with respect to time. The superposition of I_i and I_c comprises the total

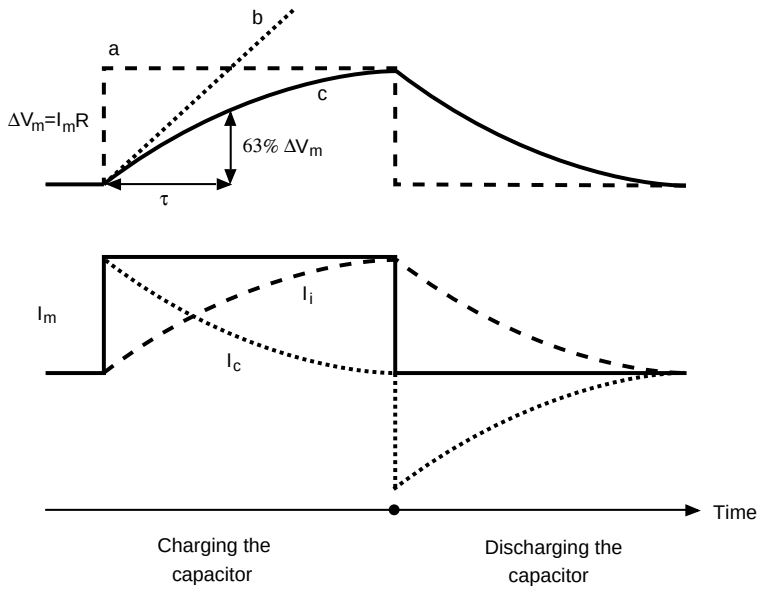

Figure C.1: Membrane potential temporal response to current perturbation.

current, I_m. This behavior is intuitive by the equation of membrane current provided above. More subtle, and important, is the behavior of membrane potential with respect to time as is given in the upper plot of Figure C.1. Membrane potential change with respect to time (plot c) is non-linear as is shown by plot c. Figure C.1 is important, however, in that it shows how the non-linear nature of potential change arrives from the interplay of resistive and capacitive properties of the membrane. Given the command current of the lower plot, line a depicts potential change behavior if the membrane contained only resistive properties. In this case the potential change would be instantaneous and maintain a constant value throughout application of the command current. Line b depicts change if the membrane were purely capacitive. Capacitive potential response is linear, and potential increases as the capacitor is charge. Once command current is released, the upper plot of Figure C.1 depicts how potential non-linearly returns to the initial level. The lower plot reveals how stored capacitor charge is released in the absence of command current. A negative current, symmetrical to the capacitive current during application of command current, is released. This current is exactly opposed by the ionic current, creating a net zero membrane current. The two plots of Figure C.1 fully specify the temporal nature of potential rate of change, showing how both resistive and capacitive properties of a neural membrane influence this change.

C.2.2 Membrane Potential Change through Space

A passive neuron behaves much like a wire cable used to transfer electricity. Ohms Law states that potential induces current. In our discussion, potential across the neural membrane induces ionic and capacitive current across the membrane, where membrane resistance, R_m, dissipates ionic current. When viewed as a cable, however, axial transfer of potential also occurs. That is, the potential at any point along the cable effects the potential at locations differentially proximal and distal to some fixed reference point. The relationship between potential, current, and resistance therefore applies spatially. Axial resistance, R_a, describes the dissipation of current induced by a potential as it propagates down the cable. As a property of conservation, current flows in the direction of least resistance. Therefore, a current applied to a point along the cable has two potential avenues of flow, ionic current across the membrane or propagation down the cable length. The following equation

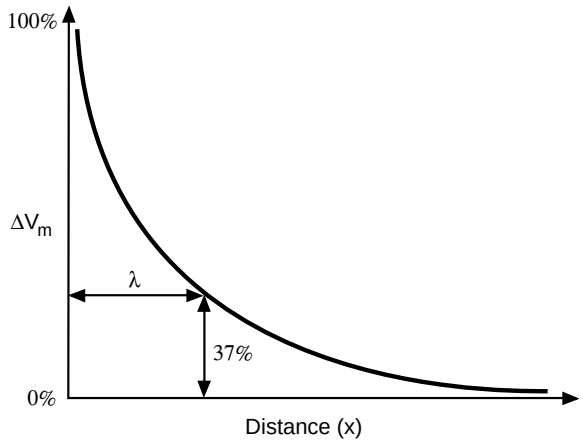

Figure C.2: Membrane potential decay with respect to spatial location.

describes potential as a function of distance.

$$\Delta V_m(x) = \Delta V_o e^{-x/\lambda}$$

where V_o denotes the potential change at some point, x_o, x is the distance from the location of command voltage, and λ is the length constant, defined by the following relationship:

$$\lambda = \sqrt{\frac{R_m}{R_a}}$$

where λ is equivalent to the distance from the point of current application where ΔV has decreased by 63%. A spatial description of potential change with respect to distance can be seen in Figure C.2.

Given these relationships governing the spatio-temporal rates of change of membrane potential, we have a clear view of passive neural membrane behavior. Passive neural behavior is most commonly seen in the dendritic branches of the neuron where voltage-gated ion channels are sparse or nonexistent.

C.3 Active Membrane Properties

We have limited our discussion to a simple neuron having only non-gated, ion selective membrane channels. Of course, this simple neuron is insufficient for describing the complex membrane potential changes of a normal neuron. Hodgkin and Huxley [12, 10, 9, 11] first explained the role of voltage-gated ion channels in neural membrane potential changes. The now legendary experiment, performed on the axon of the giant squid, mathematically elucidated the behavior of Na^+ and K^+ selective voltage-gated channels.

Hodgkin and Huxley noted the complex, non-linear path of membrane current when a command voltage was applied to the giant squid axon. A plot of this classical behavior is depicted in Figure C.3 (*Na unblocked*). Given a command voltage step, the current necessary to maintain membrane potential spikes quickly followed by a brief period of stability. This stable period then decays non-linearly before again recovering non-linearly. Hodgkin and Huxley knew *a priori* that Na^+ and K^+ ions were the dominant ionic species involved in the electro-chemical potential of the neural membrane, and they believed that the complex signature observed was actually the superposition of the Na^+ and K^+ ionic current signatures. To validate this hypothesis, they prepared the axon in an extracellular solution absent Na^+ ions. They then tested this preparation under a command voltage step identical to that of the normal neuron. Their resulting injection current trace, shown in Figure C.3 (*Na blocked*), was that of the behavior of the K^+ ions alone. Subtraction of this plot from the normal neuron plot provided the Na^+ ion current trace which is shown in Figure C.4.

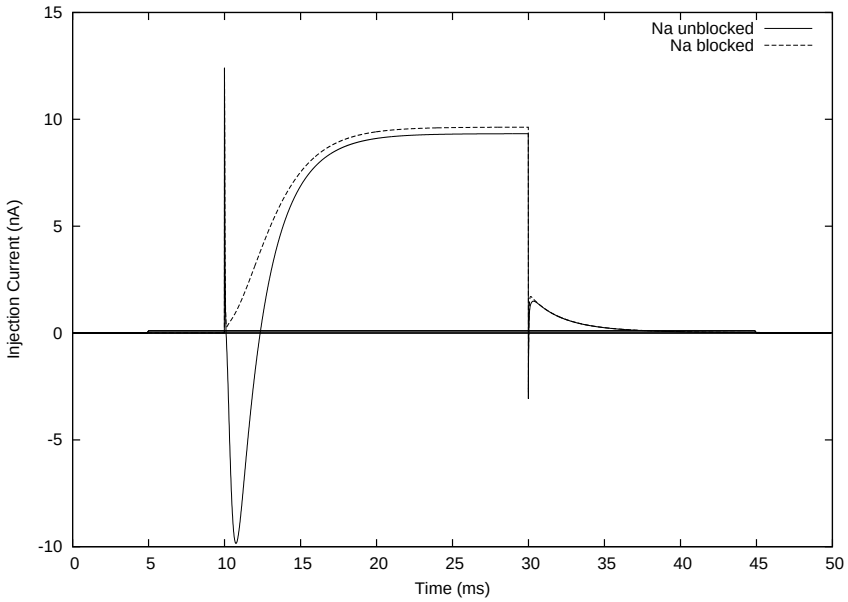

Figure C.3: Current injection applied to maintain 50 mV command voltage for 20 ms for both normal squid axon (*Na unblocked*) and squid axon with blocked Na channel.

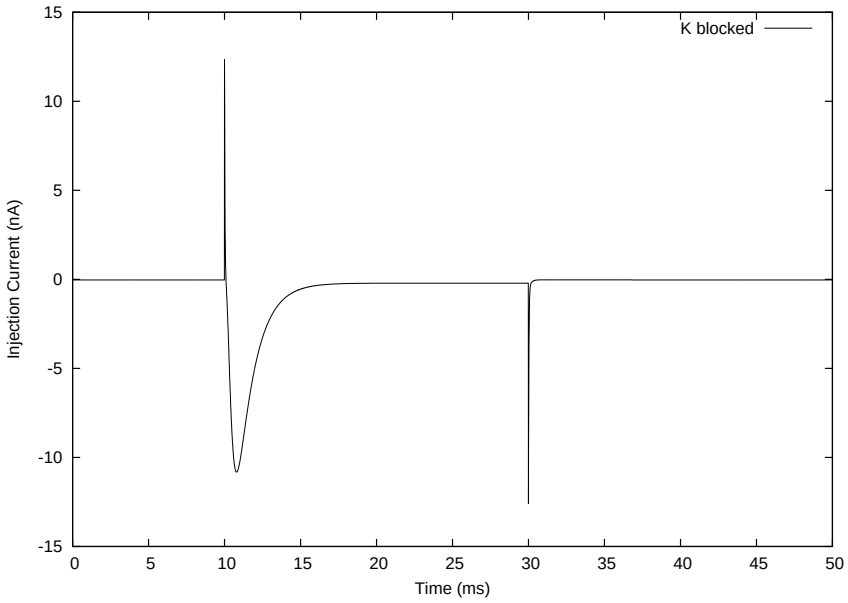

Figure C.4: Current injection applied to maintain 50 mV command voltage for 20 ms for squid axon with blocked K channel.

Decomposition of Na^+ and K^+ ionic contributions to the membrane current trace was only the initial experimental step. Hodgkin and Huxley performed similar experiments over a wide range of command voltages. Studying the differences in the current signatures, they were able to develop the functional relationship between voltage-gated ionic channel permeability and voltage. A mathematical model based on these findings, widely called the Hodgkin-Huxley model, is described below.

As we have already discussed, an ion channel is an opening in the neural membrane that permits diffusion of ionic species across the membrane barrier. Channels permit ionic passage in either direction. Channels are also selective to particular ionic species, meaning that a channel permitting Na^+ diffusion across the membrane will not permit K^+ diffusion. Non-gated ion channels freely allow passage of ionic species. More formally, non-gated ion channels have constant conductance. Ionic currents passing through these channels directly obey Ohms Law.

Voltage-gated ion channels behave much differently. The conductivity of these channels is a function of membrane potential. As the name would imply, the conductivity of these channel types is gated. Another way to think of this is that the channel itself is door that swings open freely. The gates act as a system of locks keeping the door closed to ionic passage.

Each gate has a probability, a value on the range $[0, 1]$, of being unlocked, which is referred to as the *permissive state*. A particular channel's conductivity may depend on many identical gates and any number of gate types. Formally, conductance is related to these permissive states by the following equation:

$$G_{chan} = \bar{g}_{chan} \prod_i p$$

where p is the probability of a gate being in its permissive state, G_{chan} is the absolute channel conductance per unit membrane area, and $\bar{g}_{chan}$ is the maximal channel conductance possible if all gates were in the permissive state. The product of the probabilities of a permissive state for all gates governing the channel comprises the fraction of maximal conductance possible, thus defining the absolute conductance. We will see that the probability of the permissive state for a gate is a function of voltage. However, first we should introduce practical notation. The vast majority of voltage-gated ion channels are gated by at most three unique gate types. Thus, the previous equation may be rewritten as:

$$G_{chan} = \bar{g}_{chan} p_1^{x_1} p_2^{x_2} p_3^{x_3}$$

where G_{chan} and $\bar{g}_{chan}$ are defined as previous, $p_i, i = 1, 2, 3$ are the unique gate types, and $x_j, j = 1, 2, 3$, represent the number of gates of each gate type involved in channel gating, respectively.

The rate of change of gate permissiveness with respect to time obeys first order kinetics. This is described mathematically as:

$$\frac{dp_i}{dt} = \alpha_{p_i}(1 - p_i) - \beta_{p_i} p_i$$

where α denotes the activation, or opening, of the gate, and β denotes the inactivation, or closing, of the gate. Both variables, α and β, are functions of membrane potential. Before moving on, it is important to understand this equation exactly. Given some probability of permissiveness, the rate of change of permissiveness with respect to time is increased by the activation rate times the probability of the gate being closed minus the inactivation rate times the probability of the gate being open. The probability of gate permissiveness is always on the range $[0, 1]$. Any product of a value on this range to any power will always be on the range $[0, 1]$. Therefore, even though gate permissiveness may change with respect to time, the channel conductance, as defined above will always vary over the range $[0, \bar{g}_{chan}]$.

Finally, we must specify functional descriptions of the variables α and β with respect to membrane potential. Through careful experimentation, these functions have been approximated for a wide range of voltage-gated channel types. The most commonly encountered channels have gate variables well-approximated by a common function form [4]:

$$\frac{A + Bx}{C + exp\left(\frac{x+D}{F}\right)}$$

Given that we have rates of change equations defined for the permissiveness of our gates to ionic diffusion, a question should enter your mind. These gates must have absolute values when solving for channel conductance. Yet we only have equations for rates of change. How do we solve for the values themselves? While the proper answer to this question must wait for a discussion of numerical integration methods, we can solve for gate permissiveness under equilibrium conditions. Given any membrane potential over the range defined for α and β, the steady state value of the gate permissiveness can be determined. This is achieved by setting the derivative of the gate permissiveness equal to zero and solving for the activation and inactivation values at some membrane potential, usually termed, V_{init}. Simple algebraic manipulation of the equation of rate of change yields the following equation:

$$p_{ss} = \frac{\alpha_p}{\alpha_p + \beta_p}$$

where p_{ss} is the steady state permissiveness of gate, p at some voltage, V, and α_p and βp are the activation and inactivation values of gate p at V.

Thus, given any initial membrane potential value, V_{init}, we assume the neuron is not disturbed and achieves equilibrium. Each gate variable permissiveness at this potential may be determined and used as an initial state value of the neuron. With the inclusion of voltage-gated ion channels, we have achieved a formal specification of a biologically-motivated neural membrane.

For illustration, Figure C.5 depicts mathematically modeled behavior of Na^+ and K^+ channel activation and inactivation gates for hippocampal CA3 pyramidal cells originally modeled by Traub [28]. In this diagram, the m and h gates govern the Na^+ channel conductance and the n gate controls the K^+ channel conductance. The left-hand plot depicts the rate of change of the gate activation and inactivation variables with respect to membrane potential. Rates of change are measure in ms. The most important point of this figure is to understand that gate variable rates of change are highly non-linear and vary widely. The interplay of these functions produce the complex behavior of the neuron. The right-hand plot depicts the steady state permissiveness of the gates for a range of membrane potentials. As was explained above, these values must vary over the range $[0, 1]$. The steady state plot of gate permissiveness is very powerful in determining the range of membrane potential over which the voltage-gated ion channels governed by these gates will play a role in neural decision functionality.

The importance of the understanding of voltage-gated ion channels in neural modeling cannot be understated. The complex interactions of the gate activation and inactivation equations are the most important influence in membrane potential change of an active neuron during simulation. Inherent understanding of the mathematical premises on which changes take place is crucial to successful modeling.

C.4 The Compartment Model

Now that we have developed the appropriate neurological theory to understand the mechanisms by which neurons maintain membrane potential, as well as how neural membranes respond to the introduction of external currents and potentials both temporally and spatially, we are ready to introduce a formal mathematical neural model on which realistic neural behavior may be simulated.

Canonically, the neural equivalent circuit, or *compartment model*, is used to formally diagram a section of neural membrane. The compartment model circuit incorporating all of the biological features discussed in previous sections is diagrammed in Figure C.6.

This circuit diagram represents a single neural compartment. The variables g_K, g_{Na} represent variable conductances of voltage-gated ion channels. The constant conductance g_{leak} is defined as above. R_a represents axial resistance. C_m is membrane capacitance. E_K and E_{Na} represent the

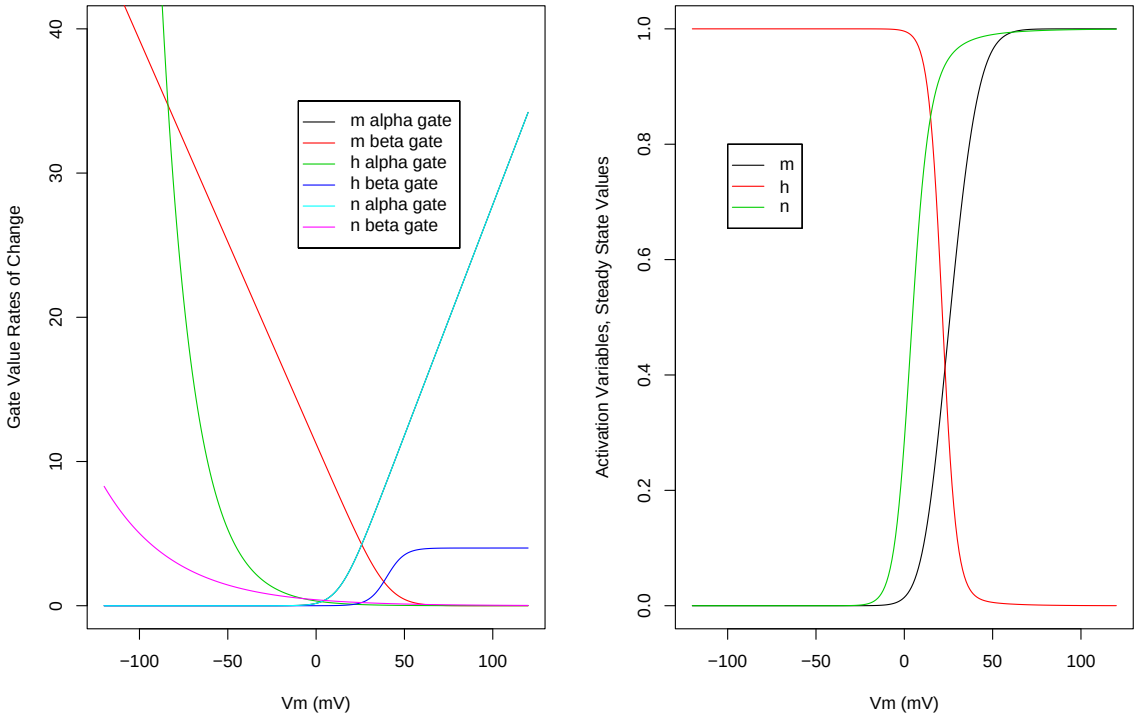

Figure C.5: Voltage dependent behavior of (*left*) gate activation and inactivation variable rates of change and (*right*) steady state permissiveness.

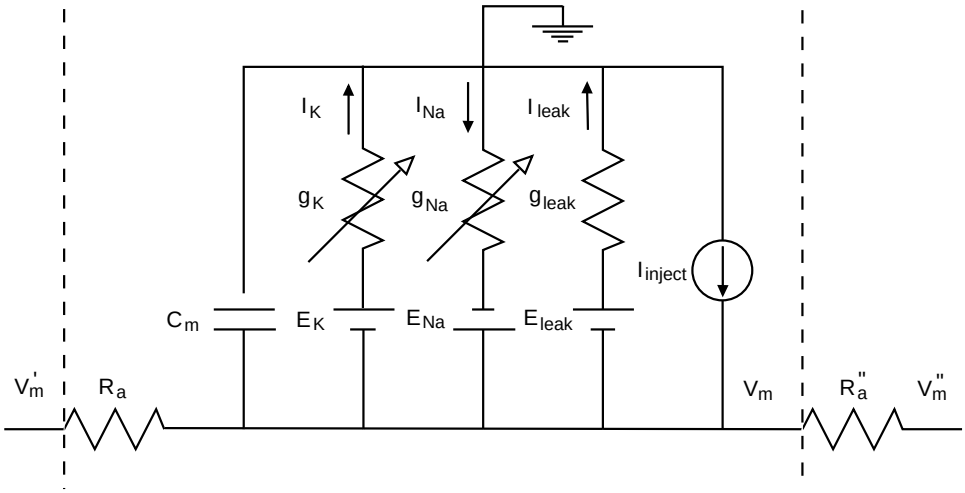

Figure C.6: Schematic of a generalized compartment model.

reversal potentials (equilibrium potentials) of K^+ and Na^+ non-gated ion channels, respectively. I_{inject} represents externally applicable current sources such as would be used in current and voltage clamp experiments. V'_m and V''_m variables are provided to illustrate the possible presence of many

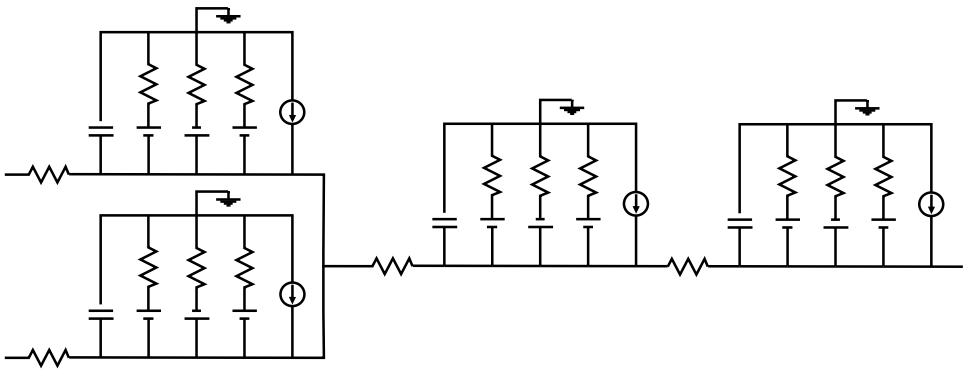

Figure C.7: Graphical representation of a complex neural membrane equivalent circuit.

such compartments. This point raises a major issue in neural modeling. Abstraction of a biological neuron to a computational model requires compartmentalization of the neuron. The number of compartments used determines the accuracy of the model. The mapping of a realistic neural membrane to a compartment model abstraction is illustrated in Figure C.7

While a neuron may be roughly approximated by one compartment, it is often advantageous to utilize many compartments connected in serial. The increase in accuracy of a multi-compartment model, however, is often complicated by the absence of realistic neural data to estimate model parameters. This is no small problem. In fact, collection of realistic data for use in parameter approximation is the single most difficult problem in neural modeling. Many of the parameters required to fully specify a computational model are unavailable. Often, parameters from similar or dissimilar neural types are the only data available. Estimation of parameters that are unknown has been labeled the "black art" of computational neuroscience. Knowing when to substitute data taken from dissimilar sources, as well as developing an intuitive feel for good approximate parameter values should be considered an important skill learned with experience. However, the incorporation of numerical analysis and machine learning techniques for optimizing model parameters given criteria of appropriate behavior should minimize the longevity of this art. Computational tools should, given a set of criteria and bounds on reasonable parameter values, be able to solve for a finite set of optimal model parameters.

Another important principle that should be highlighted here is the importance of units. Once a theoretical model is applied, units become a critical issue. The values supplied as parameters must be mutually consistent with all other values. The two most common sets of units used for neural modeling are base SI (system international) units and biological units, where biological units are a canonical subset of SI units such that model parameters have values close to single or double digits. The use of base SI units often forces parameter specification to be very large or very small such as $15 \times 10^{-6}\ m$ and so on. When incorporating units taken from many different sources, make sure the units are consistent, whatever system used.

In addition, the nature of the compartment model should be discussed. We have only described the compartment model as an approximation of neural membrane, but not really what this means. A neuron was previously related to a wire cable. For the purpose of this discussion, we consider a single compartment to model some "segment" of a real neuron. This length takes the form of a cylindrical geometry in most cases (a sphere is often used to approximate the soma). Given this, it should be known that the parameter values specified for the compartment model to this point have not incorporated spatial extent. Conductances are defined in *Siemens*. Resistances have been defined in *Ohms*. When specifying parameters for a computational compartment model, representing a real neuron, these parameters must be specified in terms relative to length, area, and volume. For example, axial resistance is the quantity $Ohms/meter$. Channel conductances are given in $Siemens/meter^2$, and so on. To scale these parameters appropriately, the neural modeler must decide how large a neural section the compartment represents and then assign appropriate units to

this geometry.

C.5 Synaptic Connectivity

The complex physiology of the synapse was discussed in Section B. Fortunately, abstraction of synaptic behavior is rather well-defined when incorporated into models at the compartment level. Almost all synaptic channels have variable conductance that are functions of time. An exception is the case of the NMDA channel which is voltage dependent through the use of an Mg^{2+} ion intermediary. In general, though, the synapse may be modeled by the following equation:

$$I_{syn} = g_{syn}(t)(V_m - E_{syn})$$

I_{syn} is the synaptic current contribution to ionic current, g_{syn} is the time-dependent synaptic conductance and E_{syn} is the reversal potential of the synaptic channel. Other variables are defined as previous. Note, the reversal of the V_m and E_{syn} terms as compared to voltage-gated ion channels. This term reversal has important ramifications for the intrinsic value of E_{syn} for each synaptic channel modeled as will be described below.

While seemingly complex, the majority of synaptic channels may be simply described by two function of time, the alpha function and the dual-exponential function. The alpha function is defined by following equation:

$$g_{syn} = g_{max}\frac{t}{\tau}(e^{1-t/\tau})$$

τ is the *time constant* and g_{max} represents the maximum possible conductance of the synapse. Given this description, the notion of *fast* and *slow* behavior is evident. A large value of τ will yield a slow acting synaptic connection. In addition, the g_{max} term will be large for a powerful connection and small for a weak connection. These relationships are depicted in Figure C.8.

The *inhibitory* or *excitatory* nature of a synapse is not primarily determined by either the g_{max} or τ term. Rather, the value and sign of the E_{syn} term has greatest influence on the synaptic connections hyperpolarizing or depolarizing influence.

When necessary to describe more complex behavior, the dual-exponential function is used, having the following form [4]:

$$g_{syn}(t) = \frac{Ag_{max}}{\tau_1 - \tau_2}\left(e^{-t/\tau_1} - e^{-t/\tau_2}\right), \tau_1 > \tau_2$$

where A is a normalizing constant and τ_1 and τ_2 represent the rising and falling *time constants*, respectively. An *AMPA* synaptic connection is well-modeled by the dual-exponential function. Typical values for this connection might be as follows: $g_{max} = 4.8 \times 10^{-9}S, E_{syn} = 0.0V, \tau 1 = 1.0ms, and \tau 2 = 1.0ms$.

C.5.1 NMDA: A voltage gated synapse

Unfortunately, not all synaptic connections commonly used in neural models are as simple as the alpha and dual-exponential functions. *NMDA*, a common slow, excitatory synaptic connection is one such exception. *NMDA* conductance is time, voltage, and concentration dependent rather than simply time dependent. The concentration dependence of *NMDA* is mediated by magnesium, $[Mg^{2+}]$, that varies among differing neural types.

Traub [28] described *NMDA* behavior for a CA3 hippocampal pyramidal cell using the following formulation.

$$g_{NMDA} = g_{ligand} \times g_{[Mg^{2+}],V_m}$$

$$g_{ligand} = g_{max}\frac{t}{\tau}(e^{1-t/\tau})$$

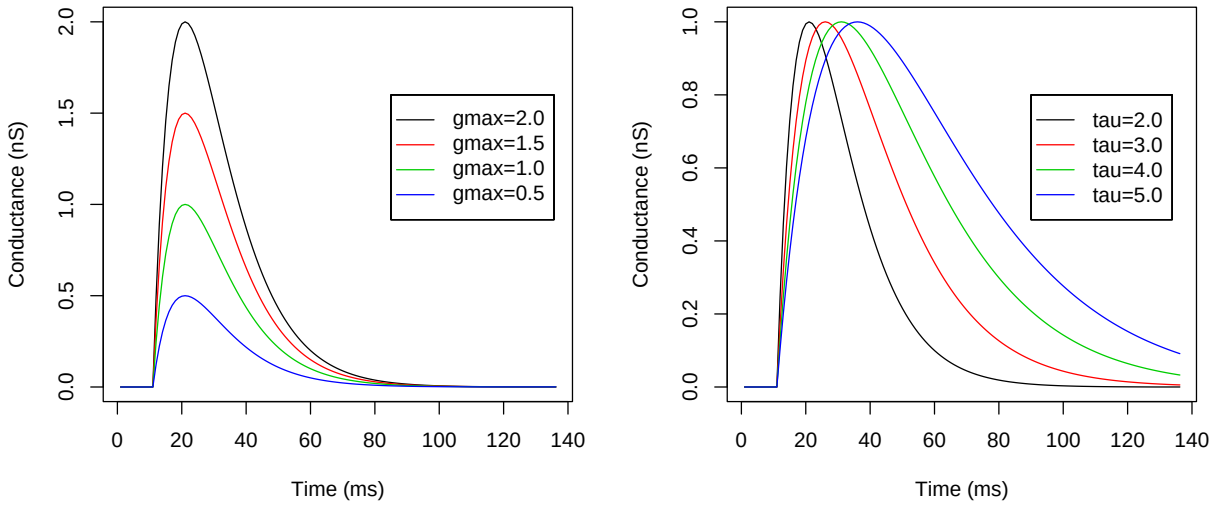

Figure C.8: Synaptic channel conductance behavior for the *alpha* function approximation when (*left*) g_{max} is varied ($\tau = 2.0$) and when (*right*) τ is varied ($g_{max} = 1.0$).

$$g_{[Mg^{2+}],V_m} = \frac{1}{1 + \frac{[Mg^{2+}]}{3} \times exp(-0.07(V_m - \xi))}$$

This example underlines the robustness and complexity of nature that must be captured in mathematical models.

C.6 Solving the Discrete Compartment Model

Given the basic mathematical theory of the separate influences on neural compartment potential, we are now ready to assemble the complete mathematical compartment representation. We begin by discussing compartment model parameters as they are often cited in research, as specific units. C_M is specific membrane capacitance, having SI units of F/m^2. R_M is specific membrane resistance having SI units of $Ohm * m^2$. R_A is specific axial resistance having units of $Ohm * m$. Specific quantities are often reported in neural modeling so that they can be studied independent of compartment dimensions, quantities that are often varied.

With specific parameters defined, it is now necessary to convert these quantities into their absolute equivalents. Equations C.5, C.6, and C.7 detail these conversions for a cylindrical compartment.

$$C_m = \Pi dl C_M \tag{C.5}$$

$$R_m = \frac{R_M}{\Pi dl} \tag{C.6}$$

$$R_a = \frac{4lR_A}{\Pi d^2} \tag{C.7}$$

From these absolute units we may redefine the description of passive cable properties representing time τ, and space, λ, constants of the cable as follows.

$$\tau = R_m C_m$$

$$\lambda = \sqrt{\frac{R_m l}{R_a / l}}$$

.

As proposed by Mascagni [15] the differential equation describing a passive cable compartment is given by:

$$\lambda^2 \frac{\delta^2 V}{\delta x^2} - \tau \frac{\delta V}{\delta t} - V = 0$$

Substitution of the λ and τ factors yields

$$\frac{R_m l^2}{R_a} \frac{\delta^2 V}{\delta^2} - R_m C_m \frac{\delta V}{\delta t} - V = 0$$

Simple algebraic manipulation yields:

$$C_m \frac{\delta V}{\delta t} = \frac{l^2}{R_a} \frac{\delta^2 V}{\delta x^2} - \frac{V}{R_m}$$

The factor $\frac{\delta^2 V}{\delta x^2}$ may then be discretized by the method of lines [15], which assumes that all compartments are of similar geometry and maintain equivalent axial resistance between compartments.

$$C_{m_i} \frac{dV_i}{dt} = \frac{l^2}{R_{a_i}} \frac{V_{i-1} - 2V_i + V_{i+1}}{(\Delta x_i)^2} - \frac{V_i}{R_{m_i}}$$

Obviously, $l = \Delta x$, therefore we may reduce the equation further:

$$C_{m_i} \frac{dV_i}{dt} = \frac{V_{i-1} - 2V_i + V_{i+1}}{R_{a_i}} - \frac{V_i}{R_{m_i}}$$

However, for compartment models in which compartment geometry and size differs, a more robust discrete approximation of the cable model may be derived:

$$C_{m_i} \frac{dV_i}{dt} = \frac{V_{i-1} - V_i}{R_{a_{i-1}}} + \frac{V_{i+1} - V_i}{R_{a_i}} - \frac{V_i}{R_{m_i}}$$

The derivation is that which is most commonly used in neural modeling. The $\frac{V_i}{R_{m_i}}$ resistance based term may be replaced by the more conventional term representing passive membrane conductance per unit area, $\bar{g}_{m_i}$, often called the leak conductance, $\bar{g}_{leak_i}$. It should be noted that if you incorporate membrane resistance based current into your calculations you cannot, realistically, introduce membrane conductance based current influences. These terms are the same and therefore represent a preference in notation. It should also be noted that the $\frac{V_i}{R_{m_i}}$ term is derived for a theoretically based compartment having a rest potential of OmV. As was discussed previously, imbalance of ions maintained by metabolic processes generates a non-zero *rest* potential for a neuron, which is labeled, E_{rest}. Thus, in a neural model in which E_{rest} is non-zero, this passive conductance term is canonically described as $\frac{(E_{leak} - V_i)}{R_{m_i}}$ yielding the generalized passive compartment model:

$$C_{m_i}\frac{dV_i}{dt} = \frac{V_{i-1}-V_i}{R_{a_{i-1}}} + \frac{V_{i+1}-V_i}{R_{a_i}} - \frac{(E_{rest}-V_i)}{R_{m_i}}$$

Adding terms for voltage-gated ion channels and externally applied current yields the overall, generalized compartment equation for potential change with respect to time, Equation C.8.

$$C_{m_i}\frac{dV_i}{dt} = \frac{V_{i-1}-V_i}{R_{a_{i-1}}} + \frac{V_{i+1}-V_i}{R_{a_i}} - \frac{(E_{rest}-V_i)}{R_m} + \sum_{chan}\bar{g}_{chan_i}(E_{chan}-V_i) + \sum_{syn}\bar{g}_{syn_i}(E_{syn}-V_i) \quad \text{(C.8)}$$

C.6.1 Numerical Integration

With a spatially discrete mathematical description in hand, the remaining question of modeling becomes one of change with respect to time. As was stated previously, the information of a neuron is not merely membrane potential, but rather how this potential changes with time. Thus, a neural model must accurately simulate membrane potential change given the above equation. To perform this simulation, we must integrate the term $\frac{dV_i}{dt}$ for each compartment with respect to time. The numerical integration process used in a neural model comprises the bulk of the computational process. Primarily, there are three numerical integration techniques used to solve the equation described above: Forward Euler, Backward Euler, and Crank-Nicolson. The first two techniques are simply opposite approximation techniques. When the term $\frac{dV_i}{dt}$ is discretized to $\frac{V_i^{n+1}-V_i^n}{\Delta t}$, the Forward Euler method requires that all voltage terms on the righthand side be described at time n, which is known

$$\begin{aligned} C_{m_i}\frac{V_i^{n+1}-V_i^n}{\Delta t} &= \frac{V_{i-1}^n-V_i^n}{R_{a_{i-1}}} + \frac{V_{i+1}^n-V_i^n}{R_{a_i}} - \frac{(E_{rest}-V_i^n)}{R_m} + \\ &\sum_{chan}\bar{g}_{chan_i}(E_{chan}-V_i^n) + \sum_{syn}\bar{g}_{syn_i}(E_{syn}-V_i^n) + I_{inject} \end{aligned}$$

This type of numerical integration is termed an explicit method, meaning only one unknown variable need be solved, that of V_i^{n+1}. The Backward Euler method is simply the opposite case. All voltage terms on the righthand side are defined for the future time step.

$$\begin{aligned} C_{m_i}\frac{V_i^{n+1}-V_i^n}{\Delta t} &= \frac{V_{i-1}^{n+1}-V_i^{n+1}}{R_{a_{i-1}}} + \frac{V_{i+1}^{n+1}-V_i^{n+1}}{R_{a_i}} - \frac{(E_{rest}-V_i^{n+1})}{R_m} + \\ &\sum_{chan}\bar{g}_{chan_i}(E_{chan}-V_i^{n+1}) + \sum_{syn}\bar{g}_{syn_i}(E_{syn}-V_i^{n+1}) + I_{inject} \end{aligned}$$

The Backward Euler method is an implicit method, as there exists more than one unknown variable to solve given one equation. Solution of an implicit method requires solving all equations for $\frac{V_i^{n+1}-V_i^n}{dt}$ simultaneously. It should be clear that for N compartments, there will exist N equations having 3 unknowns per compartment. This system of linear equations (SLE) forms a tridiagonal matrix which will be discussed in the next section. A second implicit method is the Crank-Nicolson Method which is merely the average of the Forward and Backward Euler methods. The discrete potential derivative form is as follows:

$$C_{m_i}\frac{V_i^{n+1}-V_i^n}{\Delta t} = (\frac{V_{i-1}^n-V_i^n}{R_{a_{i-1}}}+\frac{V_{i+1}^n-V_i^n}{R_{a_i}}-\frac{(E_{rest}-V_i^n)}{R_m}+$$
$$\sum_{chan}\bar{g}_{chan_i}(E_{chan}-V_i^n)+\sum_{syn}\bar{g}_{syn_i}(E_{syn}-V_i^n)+I_{inject})/2+$$
$$(\frac{V_{i-1}^{n+1}-V_i^{n+1}}{R_{a_{i-1}}}+\frac{V_{i+1}^{n+1}-V_i^{n+1}}{R_{a_i}}-\frac{(E_{rest}-V_i^{n+1})}{R_m}+$$
$$\sum_{chan}\bar{g}_{chan_i}(E_{chan}-V_i^{n+1})+\sum_{syn}\bar{g}_{syn_i}(E_{syn}-V_i^{n+1})+I_{inject})/2$$

The Forward Euler method, while fastest, is inherently unstable for all but the most prohibitively small time steps, Δt. The Backward Euler method is slow, but inherently stable for all size timesteps Δt. The Crank-Nicolson method is stable, but generally not as slow as the Backward Euler method due to its mathematical properties. The details of this stability are beyond the scope of this paper and readers are referred to Mascagni [15] for further information.

Defining these numerical integration formats, however, is not the final step. Rearrangement of terms is still necessary to place the equations in a suitable form for computational solution. A derivation of the tri-diagonal SLE follows for the Backward Euler method. Derivation of the Crank-Nicolson is similar and left as an exercise.

Given the initial Backward Euler form:

$$C_{m_i}\frac{V_i^{n+1}-V_i^n}{\Delta t} = \frac{V_{i-1}^{n+1}-V_i^{n+1}}{R_{a_{i-1}}}+\frac{V_{i+1}^{n+1}-V_i^{n+1}}{R_{a_i}}-\frac{(E_{rest}-V_i^{n+1})}{R_m}+$$
$$\sum_{chan}\bar{g}_{chan_i}(E_{chan}-V_i^{n+1})+\sum_{syn}\bar{g}_{syn_i}(E_{syn}-V_i^{n+1})$$

$$\frac{C_{m_i}}{\Delta t}V_i^{n+1}-\frac{V_{i-1}^{n+1}-V_i^{n+1}}{R_{a_{i-1}}}-\frac{V_{i+1}^{n+1}-V_i^{n+1}}{R_{a_i}}+\frac{(E_{rest}-V_i^{n+1})}{R_m}-$$
$$\sum_{chan}\bar{g}_{chan_i}(E_{chan}-V_i^{n+1})-\sum_{syn}\bar{g}_{syn_i}(E_{syn}-V_i^{n+1})=\frac{C_{m_i}}{\Delta t}V_i^n+I_{inject}$$

$$\frac{C_{m_i}}{\Delta t}V_i^{n+1}-\frac{V_{i-1}^{n+1}}{R_{a_{i-1}}}+\frac{V_i^{n+1}}{R_{a_{i-1}}}-\frac{V_{i+1}^{n+1}}{R_{a_i}}+\frac{V_i^{n+1}}{R_{a_i}}+\frac{E_{rest}}{R_{m_i}}-\frac{V_i^{n+1}}{R_{m_i}}-\sum_{chan}\bar{g}_{chan_i}E_{chan}+$$
$$\sum_{chan}\bar{g}_{chan_i}V_i^{n+1}-\sum_{syn}\bar{g}_{syn_i}E_{syn}+\sum_{syn}\bar{g}_{syn_i}V_i^{n+1})=\frac{C_{m_i}}{\Delta t}V_i^n+I_{inject}$$

$$-\frac{V_{i-1}^{n+1}}{R_{a_{i-1}}}+\left(\frac{C_{m_i}}{\Delta t}+\frac{1}{R_{a_{i-1}}}+\frac{1}{R_{a_i}}-\frac{1}{R_{m_i}}+\sum_{chan}\bar{g}_{chan_i}+\sum_{syn}\bar{g}_{syn_i}\right)V_i^{n+1}-$$
$$\frac{V_{i+1}^{n+1}}{R_{a_i}}=\frac{C_{m_i}}{\Delta t}V_i^n+\sum_{chan}\bar{g}_{chan_i}E_{chan}+\sum_{syn}\bar{g}_{syn_i}E_{syn}-\frac{E_{rest}}{R_{m_i}}+I_{inject}$$

$$\varepsilon_i=\frac{\Delta t}{C_{m_i}}$$

$$-\varepsilon_i \frac{V_{i-1}^{n+1}}{R_{a_{i-1}}} + \left(1 + \frac{\varepsilon_i}{R_{a_{i-1}}} + \frac{\varepsilon_i}{R_{a_i}} - \frac{\varepsilon_i}{R_{m_i}} + \varepsilon_i \sum_{chan} \bar{g}_{chan_i} + \varepsilon_i \sum_{syn} \bar{g}_{syn_i}\right) V_i^{n+1} -$$
$$\varepsilon_i \frac{V_{i+1}^{n+1}}{R_{a_i}} = V_i^n + \varepsilon_i \left(\sum_{chan} \bar{g}_{chan_i} E_{chan} + \sum_{syn} \bar{g}_{syn_i} E_{syn} - \frac{E_{rest}}{R_{m_i}} + I_{inject}\right)$$

$$\gamma_i = \varepsilon \left(\sum_{chan} \bar{g}_{chan_i} E_{chan} + \sum_{syn} \bar{g}_{syn_i} E_{syn} - \frac{E_{rest}}{R_{m_i}} + I_{inject}\right)$$

$$-\varepsilon_i \frac{V_{i-1}^{n+1}}{R_{a_{i-1}}} + \left(1 + \frac{\varepsilon_i}{R_{a_{i-1}}} + \frac{\varepsilon_i}{R_{a_i}} - \frac{\varepsilon_i}{R_{m_i}} + \varepsilon_i \sum_{chan} \bar{g}_{chan_i} + \varepsilon_i \sum_{syn} \bar{g}_{syn_i}\right) V_i^{n+1} - \varepsilon_i \frac{V_{i+1}^{n+1}}{R_{a_i}} = V_i^n + \gamma$$

$$\Theta_{L,i} = -\frac{\varepsilon_i}{R_{a_{i-1}}} \tag{C.9}$$

$$\Theta_{C,i} = 1 + \frac{\varepsilon_i}{R_{a_{i-1}}} + \frac{\varepsilon_i}{R_{a_i}} - \frac{\varepsilon_i}{R_{m_i}} + \varepsilon_i \sum_{chan} \bar{g}_{chan_i} + \varepsilon_i \sum_{syn} \bar{g}_{syn_i} \tag{C.10}$$

$$\Theta_{R,i} = -\frac{\varepsilon_i}{R_{a_i}} \tag{C.11}$$

$$\Theta_L V_{i-1}^{n+1} + \Theta_C V_i^{n+1} + \Theta_R V_{i+1}^{n+1} = V_i^n + \gamma_i \tag{C.12}$$

Equations C.9 through C.12, for compartments $i = 1, ..., N$ form a system of linear equations which must be solved simultaneously. However, to correctly solve these systems, an additional problem arises. The $\bar{g}_{chan}$ terms are functions of membrane potential, not simply constants. If we utilize the permissiveness rate of change equation with α and β emphasized as functions of potential:

$$\frac{dp_i}{dt} = \alpha(V)_{p_i}(1 - p_i) - \beta(V)_{p_i} p_i$$

Then we may formulate the Backward Euler integration method for this equation as: equation with α and β emphasized as functions of potential:

$$\begin{aligned} \frac{dp_i}{dt} &= \alpha_{p_i}(V_i)(1 - p_i) - \beta_{p_i}(V_i) p_i \\ \frac{p_i^{n+1} - p_i^n}{\Delta t} &= \alpha(V_i^{n+1})_{p_i}(1 - p_i^{n+1}) - \beta_{p_i}(V_i^{n+1}) p_i^{n+1} \end{aligned}$$

Algebraic manipulation will yield the following equation:

$$p_i^{n+1} = \frac{p_i^n + \Delta t \alpha_{p_i}(V_i^{n+1})}{1 + \Delta t[\alpha_{p_i}(V_i^{n+1}) + \beta_{p_i}(V_i^{n+1})]} \tag{C.13}$$

Obviously, Equation C.13 has two unknowns, that of potential and permissiveness at a future timestep. Thus, both the future potential and permissiveness must be solved iteratively by the following algorithm:

1. Compute temporary, V_i^{n+1} value using current p_i^n value.
2. Compute temporary, p_i^{n+1} value using temporary V_i^{n+1} value
3. Iterate steps 1 and 2 until the values of V_i^{n+1} and p_i^{n+1} converge (ie. step change is below some relative error value)

C.6.2 Boundary Conditions

The sealed end boundary condition, typically used in solving the types of linear systems described above, requires that no current escape out either end of the cable. This condition can be approximated by assuming the axial resistance at the end compartments approaches infinity. For compartment 1, this causes the $\Theta_{L,1}$ coefficient to be zero. For compartment N, this causes the $\Theta_{R,N}$ coefficient to be zero and the $\Theta_{C,N}$ coefficient to be described as follows:

$$\Theta_{C,N} = 1 + \frac{\varepsilon_i}{R_{a_{i-1}}} - \frac{\varepsilon_i}{R_{m_i}} + \varepsilon_i \sum_{chan} \bar{g}_{chan_i} + \varepsilon_i \sum_{syn} \bar{g}_{syn_i}$$

C.6.3 Solving Tridiagonal Matrices

For a neuron having N linearly-connected compartments, the implicit Backward Euler method generates a system of linear equations (SLE) to be solved, having a unique form called a tridiagonal matrix. A five compartment neuron SLE is depicted in Equation C.14 representing the Backward Euler numerical integration derivation described above.

$$\begin{pmatrix} \Theta_{C,1} & \Theta_{R,1} & 0 & 0 & 0 \\ \Theta_{L,2} & \Theta_{C,2} & \Theta_{R,2} & 0 & 0 \\ 0 & \Theta_{L,3} & \Theta_{C,3} & \Theta_{R,3} & 0 \\ 0 & 0 & \Theta_{L,4} & \Theta_{C,4} & \Theta_{R,4} \\ 0 & 0 & 0 & \Theta_{L,5} & \Theta_{C,5} \end{pmatrix} \begin{pmatrix} V_1^{n+1} \\ V_2^{n+1} \\ V_3^{n+1} \\ V_4^{n+1} \\ V_5^{n+1} \end{pmatrix} = \begin{pmatrix} V_1^n \\ V_2^n \\ V_3^n \\ V_4^n \\ V_5^n \end{pmatrix} + \begin{pmatrix} \gamma_1 \\ \gamma_2 \\ \gamma_3 \\ \gamma_4 \\ \gamma_5 \end{pmatrix} \tag{C.14}$$

The reason the tridiagonal matrix occurs in compartment modeling arises from the method-of-lines approximation to the second spatial derivative of potential in the cable model. Each compartment potential depends on its own potential as wells as the left and right neighboring compartments' potentials. The vector of constants arises from the BE derivation incorporating non-voltage dependent terms that are added to the current, known potential. Once in this form, any numerical stable SLE solver may be used. LU Decomposition (Gaussian elimination) is recommended [8, 15].

C.6.4 Concentration Shells

Another common compartment model abstraction is that of the concentration shell, or shell. A shell is a cylindrical volume, having a radial thickness that is measured from the compartment's membrane. This shell acts as a way to abstract the storage and transfer of ions whose concentrations are largely effected by diffusion across the membrane surface. A shell containing ionic species, S, of compartment i is defined as a concentration, $\chi_{S,i}$, an ionic conversion rate, $\phi_{S,i}$, and a concentration decay rate, $\tau_{S,i}$. The units of $\chi_{S,i}$ are $moles/m^3$. The units of $\phi_{S,i}$ are $moles/(m^3 A$ and the units of $\tau_{S,i}$ are sec. The kinetics of concentration are described by Equation C.15:

$$\frac{d\chi_{S,i}}{dt} = \phi_{S,i} I_{S,i} - \frac{\chi_{S,i}}{\tau_{S,i}} \tag{C.15}$$

where $I_{S,i}$ is the ionic current of species, S, in compartment, i. Discretizing this equation using the Backward Euler method gives the following derivation:

$$
\begin{aligned}
\frac{\chi_{S,i}^{n+1} - \chi_{S,i}^{n}}{\Delta t} &= \phi_{S,i}^{n+1} I_{S,i} - \frac{\chi_{S,i}^{n+1}}{\tau_{S,i}} \\
\frac{\chi_{S,i}^{n+1}}{\Delta t} + \frac{\chi_{S,i}^{n+1}}{\tau_{S,i}} &= \phi_{S,i}^{n+1} I_{S,i} + \frac{chi_{S,i}^{n}}{\Delta t} \\
\chi_{S,i}^{n+1} \left(\frac{1}{\Delta t} + \frac{1}{\tau_{S,i}} \right) &= \phi_{S,i}^{n+1} I_{S,i} + \frac{\chi_{S,i}^{n}}{\Delta t} \\
\chi_{S,i}^{n+1} \left(1 + \frac{\Delta t}{\tau_{S,i}} \right) &= \Delta t \phi_{S,i}^{n+1} I_{S,i} + \chi_{S,i}^{n} \\
\chi_{S,i}^{n+1} &= \frac{\Delta t \phi_{S,i}^{n+1} I_{S,i} + \chi_{S,i}^{n}}{1 + \frac{\Delta t}{\tau_{S,i}}}
\end{aligned}
\tag{C.16}
$$

Given the derived Backward Euler update, Equation C.16, solutions of $\chi_{S,i}$ for all species, S, and all compartments, i, must be addressed at each time step. Moreover, if channels are gated on value of $\chi_{S,i}$ then it must be updated during convergence of compartment potential over a timestep.

C.7 Units Conversion Tables

Relevant SI Units				
Quantity	Name	Symbol	Units	Base Units
Capacitance	Farads	F	C/V	$m^{-2}kg^{-1}s^{2}Q^{2}$
Charge	Coulombs	Q	$A * s$	Q
Conductance	Siemens	S	Ω^{-1}	$m^{-2}kg^{-1}sQ^{2}$
Current	Amperes	A	Q/s	Q/s
Length	Meters	m	m	m
Potential	Volts	V	V	$m^{2}kgs^{-2}Q^{-1}$
Resistance	Ohms	Ω	S^{-1}	$m^{2}kg^{1}s^{-1}Q^{-2}$
Time	Seconds	s	s	s